Physics – Uspekhi **69** (2) 116 – 137 (2026)

REVIEWS OF TOPICAL PROBLEMS

PACS numbers: 75.10.Jm, **74.72.–h,** 75.30.Kz, 75.50.Ee, 75.50.Gg, 75.70.Tj

Spherically symmetric approaches in the low-dimensional magnetism theory

A.F. Barabanov, V.E. Valiulin, A.V. Mikheyenkov, P.S. Savchenkov

DOI: https://doi.org/10.3367/UFNe.2025.06.039948

Contents

Abstract. The main ideas and the most important results of the spherically symmetric self-consistent approach and a number of related theoretical algorithms are presented. These methods make it possible to study low-dimensional Heisenberg-type spin models, including frustrated ones, with careful consideration of the theoretic (Mermin–Wagner and Marshall) theorems, as well as the site spin constraint. Thus, the difficulties that may arise in the traditional analysis of low-dimensional magnetic systems are avoided. The approach can also be applied to the spin-pseudospin model, and is also embedded in more complex constructions when considering spin models with free carriers, such as the basic and three-band Hubbard models, $t - J$ and $s - d$ models, and the Kondo lattice.

A.F. Barabanov (1), **V.E. Valiulin** (1, 2), **A.V. Mikheyenkov** (1, 2, *), **P.S. Savchenkov** (3, 4)
(1) Vereshchagin Institute for High Pressure Physics,
Russian Academy of Sciences,
Kaluzhskoe shosse 14, 108840 Troitsk, Moscow, Russian Federation
(2) Moscow Institute of Physics and Technology
(National Research University),
Institutskii per. 9, 141701 Dolgoprudny, Moscow region,
Russian Federation
(3) National Research Center Kurchatov Institute,
pl. Akademika Kurchatova 1, 123182 Moscow, Russian Federation
(4) National Research Nuclear University MEPhI,
Kashirskoe shosse 31, 115409 Moscow, Russian Federation
E-mail: (*) mikheen@bk.ru

Received 11 April 2025, revised 8 June 2025
Uspekhi Fizicheskikh Nauk **196** (2) 125 – 148 (2026)
Translated by I.A. Ulitkin

Keywords: low-dimensional magnetism, multi-exchange Heisenberg model, frustration, spherically symmetric approach

1. Introduction

In low-dimensional systems, including magnetic ones, the role of quantum fluctuations is significant. Frustration serves as an additional disruptive factor. Frustration in compounds with localized magnetic moments can lead to interesting and often nonintuitive effects. For example, it can lead to the formation of a nontrivial spin configuration or the loss of spin ordering even at zero temperature. Like the role of quantum fluctuations, frustration effects are particularly strong in low-dimensional, particularly two-dimensional, systems.

The description of these effects within the framework of traditional methods of magnetism theory can be difficult, which prompts the search for alternative algorithms. One such approach is the spherically symmetric self-consistent approach (SSCA) (or, in Western terminology, rotation-invariant Green's function method (RGM)).

Kondo and Yamaji [1] proposed the RGM idea for the 1D Heisenberg model half a century ago in their pioneering work. The idea is conceptually simple: in the chain of equations for two-time retarded spin-spin Green's functions, decoupling is performed not at the first step (as is traditionally done [2]), but at the second step. This scheme allows the spin state to be described not through the average spin, which can now be zero, but through spin-spin correlators.[1]

The next impetus for the development was given after the advent of high-temperature superconducting cuprates: in almost simultaneously published papers [4] and [5], the Kondo–Yamaji method was extended to the two-dimensional square Heisenberg lattice, which is relevant for cuprates. Almost immediately, a version for a frustrated lattice was developed with exchanges on the first and second neighbors [6, 7].

Subsequently, the RGM was repeatedly modified and supplemented, and was also extended to more complex models. Initially, of course, all these developments were driven by the search for a theory of high-temperature superconductivity (HTSC). Later, this self-limitation was lifted, and now this area of research can be considered quite independent and fully formed.

Below, the main ideas and some of the most important results of the RGM are presented, primarily using the example of a two-dimensional square lattice.

2. Preliminary remarks

2.1 Space dimensionality

2.1.1 3D and 1D. The RGM provides a reasonable description of the paramagnetic state of a magnetic system (the average spin at a site is zero, $\langle \hat{\mathbf{S}}_{\mathbf{i}} \rangle = 0$) with strong spin-spin correlations. Therefore, it is applicable, for example, in the three-dimensional case at temperatures slightly above the Curie or Neél temperature, of course, outside the fluctuation region.[2]

In the opposite (one-dimensional) limit, the use of the RGM is meaningless due to the existence of an exact solution. However, the RGM can be used for frustrated or so-called decorated one-dimensional systems and for several weakly coupled chains, where there is no exact solution [8–12]. The same applies to several weakly coupled planes [13–15].

2.1.2 2D. A natural domain of application for the RGM is purely two-dimensional systems. Here, two lines of research have traditionally existed: the 'line of exact theorems' and the 'line of weak three-dimensionality.'

In the first case, the basic thesis is as follows: the Mermin–Wagner theorem [16] in 2D forbids spontaneous symmetry breaking at $T > 0$; i.e., the familiar picture of a magnet with an average spin $\langle \hat{\mathbf{S}}_{\mathbf{i}} \rangle \neq 0$, directed either in one or in alternating directions, is inadequate. Furthermore, the Marshall theorem [17] requires a singlet ground state for the antiferromagnetic phase. Accordingly, standard analytical methods applicable in 3D must be modified to account for these constraints.

The second approach is based on the thesis: "strictly two-dimensional systems do not exist." Weak three-dimensionality effects are always present, which automatically rules out 2D restrictions. In the worst case, we are dealing not with long-range order, but with an exponentially large correlation length. The Marshall theorem, which is only valid at zero temperature, can be neglected entirely. Therefore, standard methods need only be modified to the extent required by the specific geometry (number of nearest neighbors, filling of coordination spheres, etc.).

The debate between these two concepts, which was quite heated during the early HTSC boom, subsequently died down, and now they peacefully coexist. Some of the basic properties of a 2D magnetic system, calculated within the framework of either concept, coincide qualitatively and semi-quantitatively. However, there are also significant differences. An analysis of these differences would take too much space and is not the purpose of this paper.

The RGM belongs to the first approach. In this approach, the state of the magnetic system — for any number and any sign of exchange interactions, at any temperature $T \geqslant 0$ — is singlet, all sites are equivalent, the average spin at a site is zero $\langle \hat{\mathbf{S}}_{\mathbf{i}} \rangle = 0$, and the spin (long-range or short-range) order is described by spin-spin correlators.

Thus, in the RGM, neither of spin nor lattice symmetry is broken.

2.2 Lattice geometry

Thus, a natural application area of the RGM is the 2D spin lattice. The next issue concerns the specific geometry of this lattice.

Lattices with geometric frustration occupy a special place, i.e., those in which the antiferromagnetic checkerboard pattern is impossible (triangular lattices, Kagome lattices, and in 3D, these are pyrochlore and hyper-Kagome lattices, etc.). In systems of this kind, the concept of chirality (the difference between right and left) and a host of other striking effects, including skyrmions, naturally arise. Research in this area is extensive and of considerable interest (see, for example, reviews [18–20] and the references therein). Here, the RGM has proven itself to be a quite effective method (triangular lattices [21–26]; Kagome lattices, including quasi-three-dimensional ones [13, 27–29]; hexagonal lattices, including quasi-three-dimensional ones [30, 31]; and pyrochlore lattices [32, 33]).

However, we will focus on another case — a square lattice (note that frustration also arises in this lattice, but for different reasons). Numerous compounds with weakly coupled square (or reducible to square planes via superexchange) magnetic planes have been experimentally studied. The best-known and best-studied are the HTSC cuprates, but, we repeat, they are by no means the only ones.

As for lattices with geometric frustration, this area deserves separate consideration, and even a brief analysis would increase the scope of this review to an unacceptable level.

---

[1] The idea of extracting spin-spin correlators from the Green's function was proposed in [3] long before Kondo and Yamaji, but there it was done at the first step after algebraic manipulations.

[2] In fact, the RGM in 3D works over a wide temperature range; for more details, see Section 12.

2.3 Spin magnitude

Thus, below we consider the application of HTSC using the example of a 2D square spin lattice. A final preliminary remark concerns the spin magnitude.

In principle, the method works for any spin (see, for example, [29, 32, 34, 35]). However, as can be shown, for the most interesting antiferromagnetic case, calculations within the RGM framework for spin $S > 1$ lead to the following: the gap in the spin excitation spectrum at the antiferromagnetic point of the Brillouin zone $\mathbf{Q} = (\pi, \pi)$ is exponentially small up to temperatures on the order of the exchange interaction. Accordingly, the correlation length is exponentially large. Although the state of the system in the RGM in this case remains singlet, all calculated quantities — the spectrum of spin excitations, the structure factor, and the magnetic susceptibility — are almost identical to those obtained using the standard spin-wave approach or approaches close to it. Thus, for large spins, the RGM, although applicable, appears to be redundant.

The case of $S = 1$ is intermediate and is also studied within the RGM framework for various lattices [24–26, 29, 32, 35, 36] (in some lattices, the case of arbitrary spin is also analyzed [29, 32]). However, the vast majority of studies consider $S = 1/2$, where the differences between the RGM results and those of the spin-wave approach (or approaches close to it) are often significant.

3. $J_1 - J_2 - J_3$ model, a sequence of complications

3.1 Hamiltonian

Thus, we consider a two-dimensional square lattice, with each site assigned a spin of $S = 1/2$ (exceptions will be discussed in Sections 10–12).

The Hamiltonian has the standard Heisenberg form, and three cases are examined: interactions between nearest neighbors only, nearest neighbors and next-nearest, neighbors on the third coordination sphere (Fig. 1a). Thus, the Hamiltonian has the form:

$$\hat{H} = J_1 \sum_{\langle \mathbf{i},\mathbf{j} \rangle} \hat{\mathbf{S}}_{\mathbf{i}} \hat{\mathbf{S}}_{\mathbf{j}} + J_2 \sum_{[\mathbf{i},\mathbf{j}]} \hat{\mathbf{S}}_{\mathbf{i}} \hat{\mathbf{S}}_{\mathbf{j}} + J_3 \sum_{\{\mathbf{i},\mathbf{j}\}} \hat{\mathbf{S}}_{\mathbf{i}} \hat{\mathbf{S}}_{\mathbf{j}} \,. \qquad (1)$$

Here $\langle \mathbf{i},\mathbf{j} \rangle$, $[\mathbf{i},\mathbf{j}]$, and $\{\mathbf{i},\mathbf{j}\}$ denote summations over pairs (bonds) of nearest-neighbor sites, second-neighbor sites, third-neighbor sites, respectively; as already mentioned, $(\hat{\mathbf{S}}_{\mathbf{i}})^2 = 3/4$.

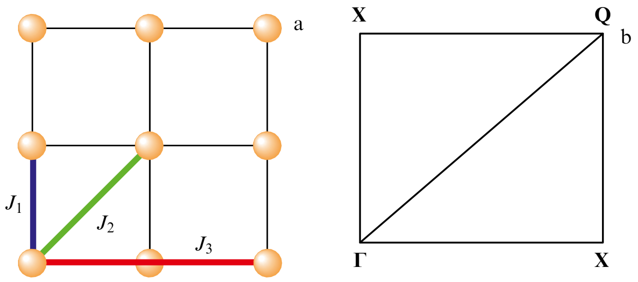

Figure 1. (a) First, second, and third nearest neighbors for a 2D square lattice and the corresponding exchange parameters. (b) Standard notations for symmetric points in the Brillouin zone of a square lattice: $\mathbf{\Gamma} = (0, 0)$ is the zero (FM) point, $\mathbf{X} = (0, \pi), (\pi, 0)$ are stripe points, and $\mathbf{Q} = (\pi, \pi)$ is the AFM point. A quarter of the full zone is shown.

3.2 Sequence of complications

The choice of a model with three exchanges is not random. At each subsequent step of increasing the complexity of the model, qualitatively new effects arise. Looking ahead, we will describe them briefly (details and references will be presented in Sections 7.1–7.3).

Model J_1. A two-dimensional antiferromagnet (AFM) and ferromagnet (FM) are described in exact accordance with the Marshall [17] and Mermin–Wagner [16] theorems. The state of the system at $T \geqslant 0$ is a singlet with zero average spin per site. There is no spontaneous symmetry breaking in spin space. In direct space, translational invariance and lattice symmetry are preserved.

At $T = 0$, long-range order arises: the modulus of the spin-spin correlator at infinity $\langle \hat{\mathbf{S}}_{\mathbf{0}} \hat{\mathbf{S}}_{\mathbf{R}} \rangle (R \to \infty)$ reaches a nonzero asymptotic value, the sign of the correlator is constant for the FM case and alternates in a checkerboard pattern in the AFM case.

Spin constraint condition $\langle \hat{\mathbf{S}}_{\mathbf{i}}^2 \rangle = 3/4$ is satisfied at each site exactly.[3] Note that in the standard spin-wave approach and similar approaches, the need to satisfy this condition is usually simply ignored; in some other approaches, for example, in the auxiliary boson method [37], the constraint is satisfied only on average over the entire system.

Model $J_1 - J_2$. All of the above mechanisms are valid. At $T = 0$, three phases with long-range order are realized: AFM, FM, and stripe phase, as well as two disordered spin-liquid phases. The loss of long-range order upon transition to a spin-liquid state is a canonical example of a quantum phase transition [38]. At $T > 0$ and for any J_1 and J_2, long-range order is absent; short-range order evolves in accordance with the structure of the zero-temperature phase.

Model $J_1 - J_2 - J_3$. In addition to the phases listed above, three different helical spin phases appear. It is significant that the helices arise without the Dzyaloshinsky–Moriya interaction ([39–42], see also the recent review [43]).

Furthermore, within a certain range of parameters, a state with two interpenetrating long-range orders is realized.

Finally, a model with more than three exchanges is difficult to justify physically. For the three previous cases considered above, physical realizations do exist.

Let us emphasize once again that the different phases and, accordingly, the phase transitions between them in the RGM occur only at $T = 0$. At $T > 0$, the state of the system is always paramagnetic, although strong correlations remain, and their structure depends on the exchange parameters.

As a side remark, note that in a triangular lattice, despite its completely different geometry, the effects arising with an increase in the number of exchanges are qualitatively similar. At $T = 0$, the inclusion of J_2 leads to new long-range-order structures as well as disordered regions; at $T > 0$, the number of distinct short-range-order structures increases. The third exchange J_3 generates incommensurate helicoidal structures [24–26].

4. Magnetic order in the classical limit

4.1 Emergence of new phases with increasing number of exchanges

Before moving to the ultraquantum limit $S = 1/2$, it is natural to consider the opposite (classical) limit $S \gg 1$.

---

[3] The term constraint has become commonly used in the RGM literature.

In this limit, on a 2D square lattice, any long-range order — commensurate or incommensurate — is described by the standard ansatz (planar helix) [44, 45]

$$\mathbf{S}_{\mathbf{r}} = \mathbf{e}_1 \cos(\mathbf{q}_0\mathbf{r}) + \mathbf{e}_2 \sin(\mathbf{q}_0\mathbf{r}) \,, \tag{2}$$

where $\mathbf{e}_1$ and $\mathbf{e}_2$ are in-plane orthogonal unit vectors (the spin length is normalized to unity here), and $\mathbf{r}$ is the radius vector of a lattice site. The point $\mathbf{q}_0$ in the Brillouin zone, which determines the magnetic order, is sometimes called the control point. A quarter of the Brillouin zone of a square lattice with the accepted notations for symmetric points is shown in Fig. 1b.

For given values of the exchange parameters J_1, J_2, and J_3, the spin structure is found by substituting (2) into (1), where the spin operators are replaced by classical vectors of unit length, and minimizing the classical energy with respect to the position of the control point $\mathbf{q}_0$.

For the J_1 model, with a unit normalization of the exchange parameter $|J_1| = 1$, the set of exchange parameter values represents two points $J_1 = \pm 1$. Substitution (2) yields a trivial result: for $J_1 > 0$, the AFM phase is realized (control point $\mathbf{q_0} = \mathbf{Q} = (\pi, \pi)$),[4] and for $J_1 < 0$, the FM phase is realized (control point $\mathbf{q_0} = \mathbf{\Gamma} = (0, 0)$).

For the $J_1 - J_2$, it is natural to use the parameterization

$$J_1 = \cos\varphi, \quad J_2 = \sin\varphi, \quad 0 \leqslant \varphi \leqslant 2\pi, \quad \sqrt{J_1^2 + J_2^2} = 1 \,. \tag{3}$$

Then the set of exchange parameter values represents a circle of unit radius. Substitution (2) leads to slightly more complex equations, whose solution reveals that, in addition to the AFM and FM phases, a stripe phase also appears. It is represented by alternating stripes with spin up and spin down. This state is doubly degenerate with respect to the two possible stripe directions. The control points for the stripe phase are $\mathbf{q}_0 = \mathbf{X} = (0, \pi), (\pi, 0)$. The regions of existence of the three phases are shown in Fig. 2a.

The $J_1 - J_2 - J_3$ model. Here, a 'spherical' parameterization is convenient[5]

$$J_1 = \cos(\psi)\cos(\varphi), \quad J_2 = \cos(\psi)\sin(\varphi), \quad J_3 = \sin(\psi),$$
$$0 \leqslant \varphi \leqslant 2\pi, \quad -\pi/2 \leqslant \psi \leqslant \pi/2, \quad \sqrt{J_1^2 + J_2^2 + J_3^2} = 1 \,. \tag{4}$$

The set of values of the exchange parameters represents a sphere of unit radius.

Substitution (2) yields rather cumbersome equations, whose solution leads to the appearance of three more phases. All possible control point positions and the corresponding values of their classical energy are listed below:

$$\begin{array}{lll}
 & \mathbf{q}_0 & E(\mathbf{q}_0) \\
\mathbf{1} & (0,0) & 4(J_1 + J_2 + J_3) \\
\mathbf{2} & (\pi,\pi) & -4(J_1 - J_2 - J_3) \\
\mathbf{3} & (0,\pi),(\pi,0) & -4(J_2 - J_3) \\
\mathbf{4} & (0,q_1),(q_1,0) & 2J_1 - \dfrac{(J_1 + 2J_2)^2}{4J_3} \,, \\
\mathbf{5} & (\pi,q_2),(q_2,\pi) & -2J_1 - \dfrac{(J_1 - 2J_2)^2}{4J_3} \\
\mathbf{6} & (q_3,q_3) & -4J_3 - \dfrac{J_1^2}{J_2 + 2J_3}
\end{array} \tag{5}$$

where the following notation is used:

$$q_1 = \arccos\left(-\frac{J_1 + 2J_2}{4J_3}\right), \quad q_2 = \arccos\left(-\frac{J_1 - 2J_2}{4J_3}\right),$$
$$q_3 = \arccos\left(-\frac{J_1}{2J_2 + 4J_3}\right). \tag{6}$$

In expressions (5), the first three phases are the already mentioned FM, AFM, and stripe structures. The remaining three phases 4–6 are spin helices (helical phases), the spins rotate from site to site, and the period of the spin structure is generally incommensurate with the lattice period.

---

[4] Sometimes, the notation $\mathbf{M}$ is used for this point in the literature.

[5] When studying local sections of the parameter domain, parameterizations other than (3) and (4) are often convenient. However, in the complete exchange domains, (3) and (4) seem to be the most adequate.

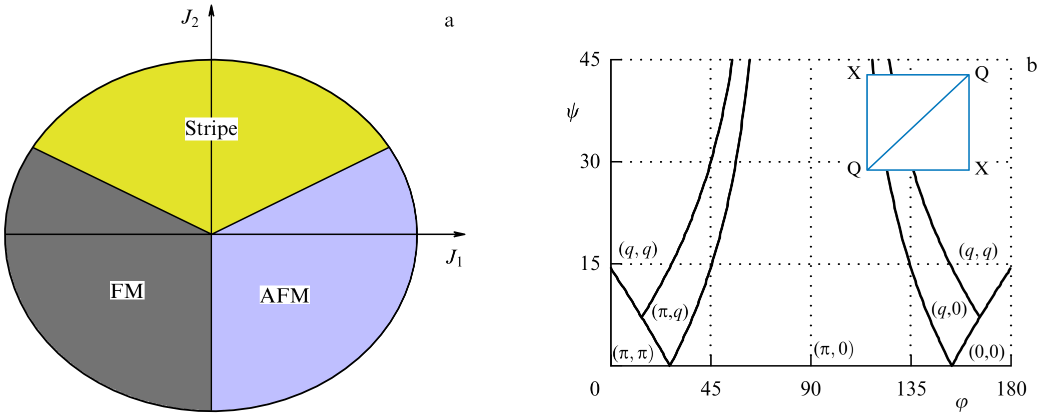

Figure 2. (a) Phase diagram of the $J_1 - J_2$ circle for a square lattice in the classical limit. AFM, stripe, and FM phases are realized. Transitions to the stripe phase occur at $0 < J_2 = \pm J_1/2$. (b) Flat scan of a portion of the phase diagram of the classical $J_1 - J_2 - J_3$ sphere, $0 \leqslant \varphi \leqslant \pi$, $0 \leqslant \psi \leqslant \pi/2$. The control point positions are shown. The inset shows a quarter of the Brillouin zone.

Figure 2b shows a flat scan of the most interesting quarter of the full sphere — the phase diagram $0 \leqslant \varphi \leqslant \pi$, $0 \leqslant \psi \leqslant \pi/2$, i.e. $1 \geqslant J_1 \geqslant -1$, $0 \leqslant J_2 \leqslant 1$, $0 \leqslant J_3 \leqslant 1$ (angles are shown in degrees.[6] All experimental data on quasi-two-dimensional compounds known to the authors fall within this region.

4.2 Features of the classical phase diagram

The following features of the phase diagram are noteworthy.

1. For FM, AFM, and stripe phases, the control point is stationary throughout the entire region of existence of the corresponding phase and abruptly changes position upon transition to another phase. For helicoids, however, as the exchange parameters change, point $\mathbf{q}_0$ moves along the symmetric lines of the Brillouin zone in accordance with (6). For helicoids Nos 4–5 from expressions (5), this movement is along the sides of the Brillouin zone, while for helicoid No. 6, it is diagonal. Thus, helicoids with a varying pitch perform a continuous transition between symmetric points.

We emphasize that, as mentioned above, in the $J_1 - J_2 - J_3$ model, spin helices arise already in the classical limit, without breaking inversion symmetry and without invoking the Dzyaloshinsky–Moriya interaction.

2. The entire region of exchange parameters can be divided into frustrated and nonfrustrated ones. In the nonfrustrated region, all exchanges operate in one direction, and all bonds are fully saturated. The simplest case is $J_1, J_2, J_3 < 0$, when all three exchanges favor the FM phase. Another example is $J_1 > 0$, $J_2 < 0$, $J_3 > 0$, with all bonds in the AFM configuration being saturated.

The literature discusses the types and extent of frustration [45] and (in the quantum case) its connection with entanglement [46–48], but we will not pursue this direction further here.

The quadrant of the full phase diagram shown in Fig. 2b is maximally frustrated — in the sense that if at least two exchanges are nonzero, then all bonds in Hamiltonian (1) cannot be simultaneously saturated. In the remaining three quadrants, this is not true for at least one of the bonds. Frustration leads to the appearance of an intermediate stripe phase between the AFM and FM phases, and, for $J_3 > 0$, frustration also leads to the appearance of helicoids. In the quantum case, the consequences of frustration are even more profound (see below).

3. The question of the experimental feasibility or fundamental nonfeasibility of specific states can be discussed. It is clear, for example, that the case $J_3 \gg J_1, J_2$ is unlikely to ever be observed experimentally. In this sense, it is significant that some helicoids arise even at small J_3 values. In general, however, this question does not admit a definitive answer.

4.3 On the quantum phase diagram

Thus, in the classical limit of the $J_1 - J_2 - J_3$ model, six spin configurations are possible: FM, AFM, stripe, and three different helices.

Within the framework of the RGM, in the ultraquantum limit of $S = 1/2$ at $T = 0$, the situation is qualitatively similar: all these long-range-order phases are possible (although the long-range order itself is described not by the average site spin, but by spin-spin correlators). However, even at $T = 0$, states without long-range order (spin liquids) may also occur. In the phase diagram, they arise between long-range-order phases in the presence of frustration.

At $T \neq 0$, long-range order is impossible; short-range order evolves with changing exchange parameters in accordance with the structure of zero-temperature phases. A detailed description is given below in Section 7.

5. Algorithm of the spherically symmetric self-consistent approach

5.1. Calculation scheme

Let us return to Hamiltonian (1). The primary calculated quantity in the RGM is the double-time retarded Green's function [49]

$$G^{zz}_{\mathbf{nm}} = \left\langle S^z_{\mathbf{n}} | S^z_{\mathbf{m}} \right\rangle_{\omega+i\delta} = -i \int_0^{\infty} \mathrm{d}t \, \exp(\mathrm{i}\omega t) \left\langle \left[S^z_{\mathbf{n}}(t), S^z_{\mathbf{m}} \right] \right\rangle . \quad (7)$$

Since a spherically symmetric state is considered, only the diagonal Green's functions $G^{zz} = G^{xx} = G^{yy}$ in the components $\alpha = x, y, z$ are nonzero (and equal to each other); there are three branches of spin excitations degenerate in α, and the average spin at the site is zero $\langle S^{\alpha}_{\mathbf{n}} \rangle = 0$.

The main idea of the RGM algorithm is to close the chain of equations of motion for the Green's function (7) at the second step. The first equation of motion in the frequency representation has the form

$$\omega\, G^{zz}_{\mathbf{nm}} = \left\langle [S^z_{\mathbf{n}}, S^z_{\mathbf{m}}] \right\rangle + \left\langle [S^z_{\mathbf{n}}, \hat{H}] | S^z_{\mathbf{m}} \right\rangle_{\omega+\mathrm{i}\delta} . \quad (8)$$

Since $\left\langle [S^z_{\mathbf{n}}, S^z_{\mathbf{m}}] \right\rangle = 0$, closure according to the traditional Tyablikov scheme at the first step [2], with the extraction of the average spin from the two-site Green's function, is impossible.[7]

The nonzero term on the right-hand side of (8) is the sum of several two-site Green's functions. Without revealing the specific form for now, we write the equation of motion for it:

$$\omega \left\langle [S^z_{\mathbf{n}}, \hat{H}] | S^z_{\mathbf{m}} \right\rangle_{\omega+\mathrm{i}\delta} = \left\langle [[S^z_{\mathbf{n}}, \hat{H}], S^z_{\mathbf{m}}] \right\rangle + \left\langle [[S^z_{\mathbf{n}}, \hat{H}], \hat{H}] | S^z_{\mathbf{m}} \right\rangle_{\omega+\mathrm{i}\delta} . \quad (9)$$

Here, the first term on the right-hand side is already nonzero, and the second term is the sum of different three-site Green's functions. From these, spin-spin correlators are extracted with closure to the original Green's function (7) (see (16) below for more details). The calculations take into account the relations arising from spherical symmetry: $\langle S^x_{\mathbf{n}} S^x_{\mathbf{n+r}} \rangle = \langle S^y_{\mathbf{n}} S^y_{\mathbf{n+r}} \rangle = \langle S^z_{\mathbf{n}} S^z_{\mathbf{n+r}} \rangle = c_{\mathbf{r}} = c_{|\mathbf{r}|}$, where $c_{\mathbf{r}}$ is the spin-spin correlator[8] at distance r.

After the Fourier transform

$$S^z_{\mathbf{q}} = \frac{1}{\sqrt{N}} \sum_{\mathbf{r}} \exp(-\mathrm{i}\mathbf{q}\mathbf{r}) S^z_{\mathbf{r}} \quad (10)$$

the solution to the system of equations (8)–(9) yields the final expression for function (7):

$$G^z(\mathbf{q}, \omega) = \left\langle S^z_{\mathbf{q}} | S^z_{-\mathbf{q}} \right\rangle_{\omega} = -\chi(\mathbf{q}, \omega) = \frac{F_{\mathbf{q}}}{\omega^2 - \omega^2_{\mathbf{q}}} \quad (11)$$

---

[6] Parametric angles are shown in degrees to avoid confusion with coordinates (radians) in the Brillouin zone.

[7] Instead of $\langle S^z_{\mathbf{n}} | S^z_{\mathbf{m}} \rangle$, one can also consider the Green's function $\langle S^+_{\mathbf{n}} | S^-_{\mathbf{m}} \rangle$, which is common for spin problems; then the requirement that the first term on the right-hand side of (8) $\langle [S^+, S^-] \rangle = 2\langle S^z \rangle$ be zero is imposed by default.

[8] To avoid misunderstanding, spherical symmetry is in spin space; in direct space, the geometry can be very different.

(hereafter, the second superscript z in the Green's function is omitted, and $\chi(\mathbf{q},\omega)$ denotes the susceptibility).

The final expressions for the numerator $F_{\mathbf{q}}$ and the spectrum of spin excitations $\omega^2_{\mathbf{q}}$ depend on the lattice geometry and the form of the Hamiltonian. But in any case, they contain spin-spin correlators on the first few coordination spheres. From simple geometric considerations, it is clear that for a square lattice in the J_1, J_1-J_2, and $J_1-J_2-J_3$ models, there are three, five, and eight such coordination spheres. Explicit (and cumbersome) expressions for $F_{\mathbf{q}}$ and $\omega^2_{\mathbf{q}}$ in the most general case are given in Section 15.

These correlators are expressed in the standard way through $G^z(\mathbf{q},\omega)$

$$c_{\mathbf{r}} = \left\langle S^z_{\mathbf{n}} S^z_{\mathbf{n+r}} \right\rangle = \frac{1}{N}\sum_{\mathbf{q}} c_{\mathbf{q}} \exp\left(\mathrm{i}\mathbf{qr}\right), \tag{12}$$

$$c_{\mathbf{q}} = \left\langle S^z_{\mathbf{q}} S^z_{-\mathbf{q}} \right\rangle = -\frac{1}{\pi}\int_0^\infty \mathrm{d}\omega \,\bigl(2m(\omega)+1\bigr)\, \mathrm{Im}\; G^z(\mathbf{q},\omega), \tag{13}$$

where $m(\omega)$ is the Bose function at a given temperature. Recall that the Bose function automatically arises in the equations for the commutator Green's function, which in itself does not imply the presence of Bose-like excitations.

The function also includes the intrasite correlator $c_{\mathbf{r}} = 0$, which is the spin constraint condition $c_{\mathbf{r}} = 0 = \langle S^z_{\mathbf{n}} S^z_{\mathbf{n}} \rangle = 1/4$.

The resulting system of self-consistent equations is then solved numerically. Note that the required computational resources are incomparably smaller than those needed for the initial first-principles numerical solution, even for a small lattice segment.

A necessary clarification to avoid misunderstandings. In the RGM, at any temperature, any number, and any sign of exchanges (including for FM), the state of the system is spherically symmetric, a singlet one. Strictly speaking, there is no mathematically impeccable proof of singletism in the RGM, since the state is not explicitly constructed. However, for any other state, it is difficult to expect the conditions for equality of correlators along the three axes, given after formula (9), to be satisfied.

5.2 Case $T = 0$

In the RGM, the zero-temperature case requires separate consideration. We will demonstrate this using the example of the AFM phase (the details vary for different phases).

At $T = 0$, long-range order arises in the system. Mathematically, this is because at $T \to 0$, a δ-shaped peak appears in the structure factor $c_{\mathbf{q}}$ (13) at the corresponding symmetric point of the Brillouin zone, in this case at the AFM point $\mathbf{Q}$. On the right-hand side of expression (13), the contribution without the Bose function is insufficient to satisfy the constraint condition. The correlator $c_{\mathbf{r}}$ necessarily takes the form

$$c_{\mathbf{r}} = \frac{1}{N}\sum_{\mathbf{q}} c_{\mathbf{q}} \exp\left(\mathrm{i}\mathbf{qr}\right) + c^{\mathrm{afm}}_{\mathrm{cond}} \exp\left(\mathrm{i}\mathbf{Qr}\right). \tag{14}$$

Here, $c^{\mathrm{afm}}_{\mathrm{cond}}$ is the modulus of the spin-spin correlator at infinity (the so-called spin condensate), and the correlator itself changes sign in a checkerboard pattern

$$\langle S^\alpha_{\mathbf{0}} S^\alpha_{\mathbf{r}} \rangle^{\mathrm{afm}}_{\mathbf{r}\to\infty} = c^{\mathrm{afm}}_{\mathrm{cond}} (-1)^{n_x+n_y}, \;\; \alpha = x,y,z, \;\; \mathbf{r} = n_x\mathbf{g}_x + n_y\mathbf{g}_y\,. \tag{15}$$

Otherwise, the calculation scheme remains the same; $c^{\mathrm{afm}}_{\mathrm{cond}}$ becomes an additional self-consistency parameter.

The above reasoning may seem insufficiently rigorous. A more accurate justification can be found, for example, in [50].

Generally speaking, a detailed consideration of the $T = 0$ case is necessary primarily for completeness, to demonstrate that the method also works at zero temperature, where "Bose condensation of spin excitations" occurs, or to solve specific problems, such as those concerning quantum phase transitions. Most essential conclusions, including phase boundaries with long-range order, can be obtained by extrapolating low-temperature results. Therefore, in what follows, the zero-temperature case will be occasionally omitted.

5.3 Vertex corrections

In the RGM, beginning with the pioneering papers [1, 4–7], so-called vertex corrections have been introduced (the term is not directly related to diagrammatic technique). The introduction of the correction leads to renormalization of the spin-spin correlator when extracting it from the three-site Green's function

$$\begin{aligned}\left\langle S^\alpha_{\mathbf{l}} S^\alpha_{\mathbf{l+r}} S^z_{\mathbf{n}} | \ldots \right\rangle \to \alpha_r \left\langle S^\alpha_{\mathbf{l}} S^\alpha_{\mathbf{l+r}} \right\rangle \left\langle S^z_{\mathbf{n}} | \ldots \right\rangle = \alpha_r c_r \left\langle S^z_{\mathbf{n}} | \ldots \right\rangle \\ = \tilde{c}_r \left\langle S^z_{\mathbf{n}} | \ldots \right\rangle.\end{aligned} \tag{16}$$

In all expressions where such extraction occurs, the renormalized correlators $\tilde{c}_r$ are used (details can be found in the literature cited above).

Vertex corrections depend on the lattice vector r, and, in principle, each coordination sphere can have its own α_r (three, five, or eight, respectively, for the J_1, J_1-J_2 and $J_1-J_2-J_3$ models). The simplest single-vertex configuration (all vertices coincide) is sufficient to satisfy the constraint condition, and even in this case, all the main results are reproduced.

More complex adjustments are made based on various reasonable physical considerations; details can be found in the aforementioned papers. With increasing temperature, all corrections $\alpha \to 1$. At low temperatures, in most studies, the vertex corrections do not deviate far from unity, and $\alpha \leqslant 1.5$.

The presence of vertex corrections should be kept in mind when comparing results from different studies. For the same model, calculated quantities always agree qualitatively and semiquantitatively, but may differ strictly quantitatively due to different vertex selection.

6. Advantages and disadvantages of the spherically symmetric self-consistent approach

The previous sections described the spherically symmetric self-consistent approach for double-time retarded spin Green's functions, whose main application is low-dimensional magnetic systems. We now list the main advantages and disadvantages of the RGM. Let us start with the disadvantages.

Disadvantages.

1. Despite some sophistication and cumbersomeness, the RGM is still a mean-field approach. It does not allow one to determine the damping of spin excitations within its basic formulation. Progress in this direction is only possible through semi-phenomenological renormalizations or other complications.

2. The RGM is a method with uncontrollable accuracy. Although the error can often be estimated using various secondary considerations, such estimates are not intrinsic to the method. As a rule, there is no small parameter (however, this situation is common for magnetic problems).

3. The method includes one or more tuning parameters (vertex correction).

4. The studied state is not structurally constructed; it is described via the Green's function, spin correlators, structure factor, and excitation spectrum. Although, strictly speaking, this can hardly be considered a significant drawback.

5. A local limitation arises in the spin-liquid region [generally, there are several of them, but the one located between the AFM and stripe phases has been better studied (see Fig. 3)]. Methods based on resonating valence bond (RVB) concept, depending on the exchange parameters, reveal multiple structures here, differing in higher-order correlators (see, for example, reviews [19, 51] and the references therein), whereas the RGM describes this region as a single phase without long-range order with evolving short-range order.

Advantages.

1. The RGM satisfies the Mermin–Wagner and Marshall theorems, as well as the exact spin constraint at each site.

2. At $T = 0$, the method allows one to analyze states with and without long-range order.

3. Over a wide temperature range $T > 0$, a single approach reproduces all possible short-range-order structures in the system.

4. The RGM allows one to calculate the spin excitation spectrum $\omega_{\mathbf{q}}$, the dynamic susceptibility $\chi(\mathbf{q}, \omega, T)$, the structure factor $c_{\mathbf{q}}$, energy, and heat capacity. Crucially, no initial assumptions are made about the form of the spin excitation spectrum; the spectrum is determined through self-consistency.

5. The method can be embedded into more complex constructions when considering spin models with free carriers, such as the basic and three-band Hubbard models, the $t-J$ and $s-d$ models, and the Kondo lattice (see Section 11 and references therein).

6. In many local regions of the phase diagram, the RGM results agree with numerical simulations (see Section 7.2.3 and references therein).

7. Results for a square lattice

The basic ideas and the standard computational algorithm of the RGM were outlined above using a two-dimensional square lattice as an example. This section presents the main RGM results for three versions of the Heisenberg model on a square lattice: J_1, $J_1 - J_2$ and $J_1 - J_2 - J_3$ (with spin $S = 1/2$ throughout this section).

The focus in this section is placed primarily on the results concerning the spin structure: the structure factor, short- and long-range magnetic order, the spin excitation spectrum, and the evolution of all these quantities with temperature and exchange parameters.

Magnetization, magnetic susceptibility, and heat capacity are discussed only insofar as necessary to demonstrate the applicability of the method. Analytically tractable limits or, conversely, the fitting of numerical data to simple functional relationships are not be systematized, as these topics are extensively covered in the cited literature. A detailed discussion would shift the focus of this review and significantly increase its length.

7.1 J_1 model

The most important result of the RGM for the model with the nearest-neighbor exchange [4, 5] is the very possibility of describing the spin structure in terms of a singlet space for both the FM and AFM cases at temperatures $T \geqslant 0$. In both cases, the average spin at each site is zero, and the constraint condition $\langle \hat{\mathbf{S}}_{\mathbf{i}} \rangle = 0$, $\langle \hat{\mathbf{S}}_{\mathbf{i}}^2 \rangle = 3/4$ is exactly satisfied. The spin-spin correlator $\langle S_{\mathbf{0}}^{\alpha} S_{\mathbf{r}}^{\alpha} \rangle$ is independent of α, i.e., $\langle S_{\mathbf{0}}^{x} S_{\mathbf{r}}^{x} \rangle = \langle S_{\mathbf{0}}^{y} S_{\mathbf{r}}^{y} \rangle = \langle S_{\mathbf{0}}^{z} S_{\mathbf{r}}^{z} \rangle$, and the three branches of spin excitations are degenerate.

FM exchange $J = -1$.

At $T = 0$, the structure factor $c_{\mathbf{q}}$ exhibits a δ-shaped peak at the zero point of the Brillouin zone $\boldsymbol{\Gamma} = (0, 0)$. The spin-spin correlator $\langle S_{\mathbf{0}}^{\alpha} S_{\mathbf{r}}^{\alpha} \rangle$ is positive and approaches a constant value as $\mathbf{r} \to \infty$ (the FM correlation length is infinite)

$$T = 0, \quad \langle S_{\mathbf{0}}^{\alpha} S_{\mathbf{r}}^{\alpha} \rangle_{\mathbf{r} \to \infty} \to \text{const}, \quad \alpha = x, y, z\,. \tag{17}$$

For the studied state with zero average spin, the constant in (17), the so-called effective magnetization m, characterizes the spin structure:

$$m = \left(\lim_{\mathbf{r} \to \infty} \left| \langle \mathbf{S_0 S_r} \rangle \right| \right)^{1/2}, \tag{18}$$

within the RGM for the FM case, one obtains $m = 1/2$, as expected.

The spin excitation spectrum is close to the standard spin-wave spectrum (small differences depend on the choice of vertex corrections), and the gap is closed only at point $\boldsymbol{\Gamma}$.

At $T > 0$, the spectrum evolves, but no qualitative changes are observed. However, the height of the peak $c_{\mathbf{q}}$ becomes finite, and its width now defines a finite correlation length. The spin-spin correlator decreases to zero asymptotics with increasing r

$$T > 0, \quad \langle S_{\mathbf{0}}^{\alpha} S_{\mathbf{r}}^{\alpha} \rangle_{\mathbf{r} \to \infty} \to 0, \quad \alpha = x, y, z\,. \tag{19}$$

Thus, the RGM provides a description of a singlet state with a finite correlation length and strong FM correlations.

AFM exchange $J = +1$.

At $T = 0$, the δ-shaped peak of the structure factor $c_{\mathbf{q}}$ is located at the AFM point of the Brillouin zone $\mathbf{Q} = (\pi, \pi)$. The spin-spin correlator alternates in sign (checkboard pattern), and its modulus becomes constant as $\mathbf{r} \to \infty$ (the AFM correlation length is infinite)

$$T = 0, \quad \left| \langle S_{\mathbf{0}}^{\alpha} S_{\mathbf{r}}^{\alpha} \rangle \right|_{\mathbf{r} \to \infty} \to \text{const}, \quad \alpha = x, y, z\,. \tag{20}$$

The effective magnetization in (20) for the AFM case is nonzero and equal to $m = 0.3$, in agreement with the results obtained using many alternative analytical and numerical approaches, including two-sublattice approaches [52]. This agreement provides additional support for the validity of the RGM.

As in the FM case, the spin excitation spectrum is close to the standard spin-wave spectrum (minor differences depend on the choice of vertex corrections), with the gap closed at the zero point $\boldsymbol{\Gamma} = (0, 0)$ and at the AFM point $\mathbf{Q} = (\pi, \pi)$.

At $T > 0$, the peak height of $c_{\mathbf{q}}$ becomes finite, the spin-spin correlator decreases to zero asymptotics with increasing r, and the correlation length becomes finite

$$T > 0, \quad \langle S_{\mathbf{0}}^{\alpha} S_{\mathbf{r}}^{\alpha} \rangle_{\mathbf{r} \to \infty} \to 0, \quad \alpha = x, y, z\,. \tag{21}$$

However, unlike the FM case, the spectrum undergoes a qualitative change at finite temperature. Specifically, the gap opens and increases with increasing temperature at the AFM point $\mathbf{Q} = (\pi, \pi)$.

This is one of the key differences between the RGM and the spin-wave and related approaches. The spherically symmetric approach makes it possible to describe the singlet state of a system with strong AFM correlations.

The mathematical reason for this is as follows: translational symmetry is not broken In the RGM, and no lattice doubling occurs in the AFM case. The analysis is carried out in the full (not reduced magnetic) Brillouin zone, where the points $\mathbf{Q} = (\pi, \pi)$ and $\mathbf{\Gamma} = (0, 0)$ are inequivalent.

7.2 $J_1 - J_2$ model

The $J_1 - J_2$ model has been extensively studied in the literature [6, 7, 53–62] (early reviews of some ideas in this area can be found in [63, 64]).

The initial motivation for investigating this model was, of course, related to HTSC cuprates, in which the spin subsystem is quasi-two-dimensional and possesses square symmetry. More than fifteen compounds have been identified in which experiments indicate frustrated $J_1 - J_2$ magnetism [65–82]. In addition to the HTSC cuprates, these include, for example, $Pb_2VO(PO_4)_2$, $(CuCl)LaNb_2O_7$, $SrZnVO(PO_4)_2$, $BaCdVO(PO_4)_2$, K_2CuF_4, Cs_2CuF_4, Cs_2AgF_4, La_2BaCuO_5, Rb_2CrCl_4, and others.

These compounds fill the entire upper half of the $J_1 - J_2$ circle [59, 60, 62, 83]. Moreover, many of them are characterized by frustration leading to suppression of long-range order [71, 72, 74–79].

Two further clarifications are necessary.

First. Early work on the $J_1 - J_2$ model was motivated by the idea of reproducing the magnetic properties of HTSC cuprates. Some of these attempts were made to describe the experimentally observed ‘subtle properties’ of the spin spectrum of HTSC cuprates, such as the so-called ‘resonance mode’ or ‘hour-glass spectrum’ (see [84] for details). To this end, additional parameters and considerations were introduced into the standard scheme. We will not go into such details here, and below we will present the basic, fundamental properties of the spin spectra in the $J_1 - J_2$ model.[9]

Second. For the same reason — the description of HTSC, many studies considered theoretical models containing both a magnetic background and charge carriers (interacting with it). This area is beyond the scope of this review and will be only briefly mentioned in Section 11.

Before proceeding to a systematic description of the possible spin structures in the $J_1 - J_2$ model, several general introductory remarks are necessary.

At $T = 0$, the structure factor $c_{\mathbf{q}}$ can either contain a δ-shaped contribution or be finite throughout the Brillouin zone. In the former case, this is a phase with long-range order, the structure of which is determined by the peak position. In the latter case, it is a spin-liquid phase without long-range order, with the short-range order being determined by the structure factor profile.

At $T \neq 0$, long-range order is impossible in the RGM under any exchange conditions, and $c_{\mathbf{q}}$ is finite everywhere. The point $\mathbf{q}_0$ — the position of the maximum of the structure factor in the Brillouin zone — determines the structure of the short-range order, and the half-width of the $c_{\mathbf{q}}$ peak defines the correlation length relative to the corresponding order (ignoring equivalent points in the full Brillouin zone). Thus, the point $\mathbf{q}_0$ is the quantum analogue of the control point in the classical model.

7.2.1 Spin order at zero temperature

7.2.1 Spin order at zero temperature. At $T = 0$, depending on the ratio of exchange interactions, five distinct spin structures are realized: three phases with long-range order (AFM, stripe, and FM) and two spin-liquid regions (Fig. 3). As one moves along the $J_1 - J_2$ circle, a cascade of quantum phase transitions occurs.

The evolution of spin-spin correlators over the entire $J_1 - J_2$ circle is shown in Fig. 4. Gaps in the spin excitation spectrum at symmetric points of the Brillouin zone are presented in Fig. 5. The trigonometric parameterization of the exchanges introduced in Section 4.1 is used: $J_1 = \cos\varphi$, $J_2 = \sin\varphi$, $0 \leqslant \varphi \leqslant 2\pi$, $[J_1^2 + J_2^2]^{1/2} = 1$.[10]

Upper half of the J_1–J_2 circle.

0 → SL_1. On the upper semicircle, between $\varphi = 0$ and the lower boundary of the spin-liquid phase SL_1, the *AFM phase with long-range order* is realized. The structure factor $c_{\mathbf{q}}$ has a δ-shaped peak at the AFM point of the Brillouin zone $\mathbf{Q} = (\pi, \pi)$. The gap in the spin excitation spectrum at point $\mathbf{Q}$ is closed[11]. The spin-spin correlator modulus at infinity becomes constant, and its sign changes in a checkerboard pattern

$$\langle S_{\mathbf{0}}^{\alpha} S_{\mathbf{r}}^{\alpha} \rangle_{\mathbf{r}\to\infty}^{\mathrm{afm}} = c_{\mathrm{cond}}^{\mathrm{afm}} (-1)^{n_x+n_y}, \ \alpha = x, y, z, \ \mathbf{r} = n_x \mathbf{g}_x + n_y \mathbf{g}_y \,. \tag{22}$$

As φ increases, the spin condensate $c_{\mathrm{cond}}^{\mathrm{afm}}$ decreases, and a quantum phase transition to a *spin liquid without long-range order* occurs at point SL_1.

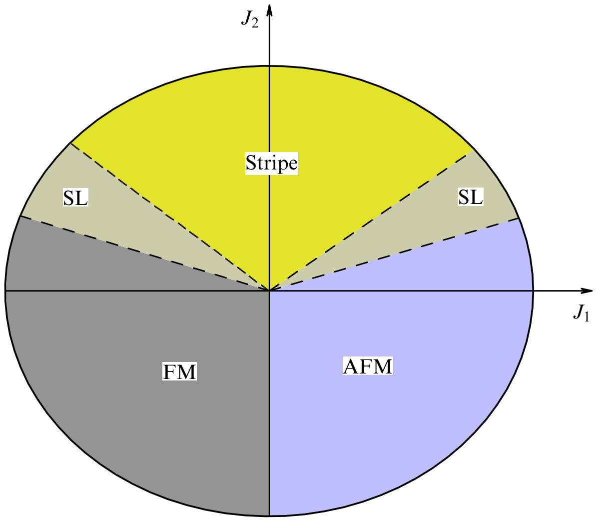

Figure 3. Schematic of the quantum $S = 1/2$ $J_1 - J_2$ model at $T = 0$. A disordered spin-liquid (SL) phase is realized between the AFM and stripe phases with long-range order. A second spin-liquid region appears between the FM and stripe long-range orders. The spin-liquid boundaries are shown tentatively, without exact correspondence to the calculated data.

---

[9] Most of the quantitative results in this section correspond to the standard implementation of the RGM in the single-vertex approximation.

[10] All energy quantities in this section (except Fig. 7) are normalized to $[J_1^2 + J_2^2]^{1/2}$.

[11] As in the J_1 model, the gap at the zero point $\mathbf{\Gamma} = (0, 0)$ in $J_1 - J_2$ is closed at any temperature and any exchanges.

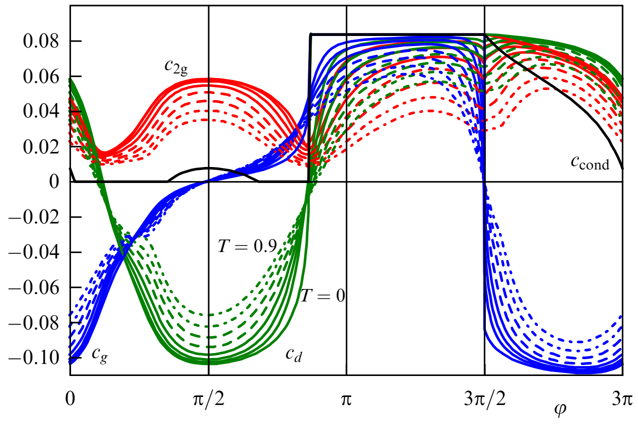

Figure 4. J_1-J_2 model. Spin–spin correlators at the nearest neighbors (c_g, blue), second nearest neighbors (c_d, green), and third nearest neighbors (c_{2g}, red) as functions of parametric angle φ ($J_1 = \cos\varphi$, $J_2 = \sin\varphi$). The thick solid lines correspond to the temperature $T = 0$; the thin solid lines, to $T = 0.3$, 0.4, and 0.5; the dashed lines, to $T = 0.6$, and 0.7; and the dotted lines, to $T = 0.8$ and 0.9. The spin condensate c_{cond} (on a different scale) is shown by the solid black line. The trigonometric parameterization of the exchanges is $J_1 = \cos\varphi$, $J_2 = \sin\varphi$, $\varphi \leqslant 2\pi$, $[J_1^2 + J_2^2]^{1/2} = 1$. (Data from [62].)

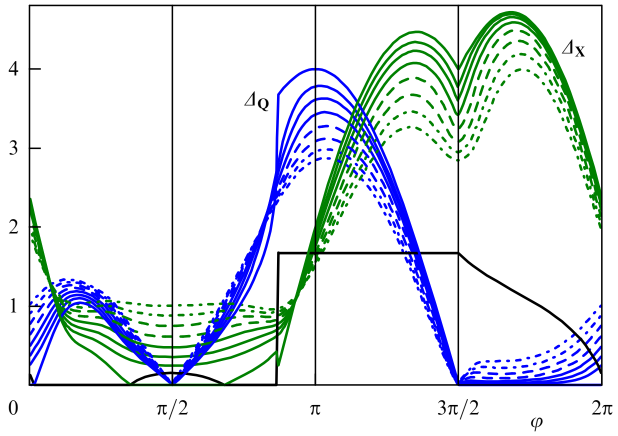

Figure 5. Gaps in the spectrum of spin excitations $\Delta_{\mathbf{Q}}$ (blue) and $\Delta_{\mathbf{X}}$ (green) at symmetric points of the Brillouin zone $\mathbf{Q} = (\pi, \pi)$ and $\mathbf{X} = (0, \pi), (\pi, 0)$ as functions of parametric angle φ ($J_1 = \cos\varphi$, $J_2 = \sin\varphi$). The thick solid lines correspond to temperature $T = 0$; the thin solid lines, to $T = 0.3, 0.4$, and 0.5; the dashed lines, to $T = 0.6$ and 0.7; and the dotted lines, to $T = 0.8$ and 0.9. The spin condensate c_{cond} (on a different scale) is shown as a solid black line. (Data from [62].)

$\text{SL}_1 \to \text{SL}_2$. In a spin liquid, the peak in the structure factor at point $\mathbf{Q}$ becomes finite, with its width determining the correlation length. The gap in the spectrum at point $\mathbf{Q}$ is open, but small. Short-range order retains the AFM structure (see Fig. 4); the nearest-neighbor correlator is $c_g < 0$, and the next-nearest and third-neighbor correlators are $c_d > 0$ and $c_{2g} > 0$, respectively.

With increasing φ when moving from SL_1 to the upper boundary of the spin liquid SL_2, the gaps decrease, and the maxima of the structure factor at the stripe points of the Brillouin zone $\mathbf{X} = (0, \pi), (\pi, 0)$ increase. At the AFM point, on the contrary, the gap increases, and the peak of $c_{\mathbf{q}}$ decreases. Thus, short-range order evolves towards the stripe structure. At the upper boundary of the spin liquid SL_2, a quantum phase transition to the *stripe phase with long-range order* occurs.

$\text{SL}_2 \to \text{SL}_3$. This is the stripe phase region. The structure factor exhibits a δ-shaped peak at the stripe points of the Brillouin zone $\mathbf{X} = (0, \pi), (\pi, 0)$. The gap in the spectrum of spin excitations at the points X is closed. The modulus of the spin-spin correlator at infinity approaches a constant value. In the RGM, the stripe phase is a quantum superposition of horizontal and vertical stripes, and the correlator at infinity has the form

$$\langle S_{\mathbf{0}}^{\alpha} S_{\mathbf{r}}^{\alpha}\rangle^{\text{stripe}}_{\mathbf{r}\to\infty} = c^{\text{stripe}}_{\text{cond}}\,\frac{1}{2}\left[(-1)^{n_x} + (-1)^{n_y}\right], \quad \alpha = x, y, z,$$
$$\mathbf{r} = n_x \mathbf{g}_x + n_y \mathbf{g}_y\,. \tag{23}$$

The point $\varphi = \pi/2$ of the J_1-J_2 circle is highlighted. It corresponds to $J_1 = 0$, $J_2 = 1$. From geometric considerations, it is obvious that during such exchanges, the lattice splits into two diagonally shifted, noninteracting sublattices. This leads, for example, to a divergence of the magnetic susceptibility. An arbitrarily small value of $J_1 \neq 0$ eliminates the divergence.[12]

As φ increases, the magnitude of the spin condensate $c^{\text{cond}}_{\text{stripe}}$ decreases, and the next quantum phase transition occurs at point SL_3 — to the *second spin-liquid region without long-range order*.

$\text{SL}_3 \to \text{SL}_4$. In the second spin liquid region, the peaks of the structure factor at the stripe points of the Brillouin zone become finite, as does the correlation length. The gaps at the $\mathbf{X}$ points are open. Short-range order retains the stripe structure (see Fig. 4), characterized by $c_d < 0$, $c_{2g} > 0$ and the sign of c_g can change.

With further increase in φ, when moving from SL_3 to SL_4, the maximum of the structure factor at the zero point of the Brillouin zone $\mathbf{\Gamma} = (0, 0)$ increases (the gap in the spectrum at this point is always closed). Short-range order evolves toward the FM structure.

At point SL_4, another quantum phase transition occurs — to the *long-range-order FM region*.

$\text{SL}_4 \to \pi$. FM region. The δ-shaped peak of the structure factor at the zero point of the Brillouin zone $\mathbf{\Gamma} = (0, 0)$ (the gap is also closed there). All spin-spin correlators are positive. The correlator at infinity approaches a constant sign of $c^{\text{cond}}_{\text{fm}}$.

Lower half of the J_1-J_2 circle.

The lower semicircle is of no experimental interest — no known materials correspond to the regions $J_1 < 0$, $J_2 < 0$ (third quadrant, $\pi < \varphi < 3\pi/2$) or $J_1 > 0$, $J_2 < 0$ (fourth quadrant, $3\pi/2 < \varphi < 2\pi$) were detected.

From a theoretical perspective, this region is also not very interesting due to the absence of frustration: in the third quadrant, both exchanges favor the FM phase, while in the fourth quadrant, they favor the AFM phase. The only noteworthy feature is the transition at $\varphi = 3\pi/2$, when the correlator at the nearest neighbors changes its sign in a jump-like manner.

7.2.2 Spin structure at finite temperature.

At $T > 0$, there is no long-range order in the RGM for any exchanges. The spin-spin correlators are zero at infinity. The gaps in the spectrum at the symmetric points of the Brillouin zone are open [except

---

[12] Moreover, at the point $\varphi = \pi/2$ and the opposite point $\varphi = 3\pi/2$, the gap $\Delta_{\mathbf{Q}}$ is closed for any T (see Fig. 5). Formally, this follows from the analytical expression for $\Delta_{\mathbf{Q}}$. The physical explanation is that the system of two noninteracting sublattices is degenerate with respect to their mutual rotation. Therefore, the transfer of spin excitation to an adjacent site does not require any energy.

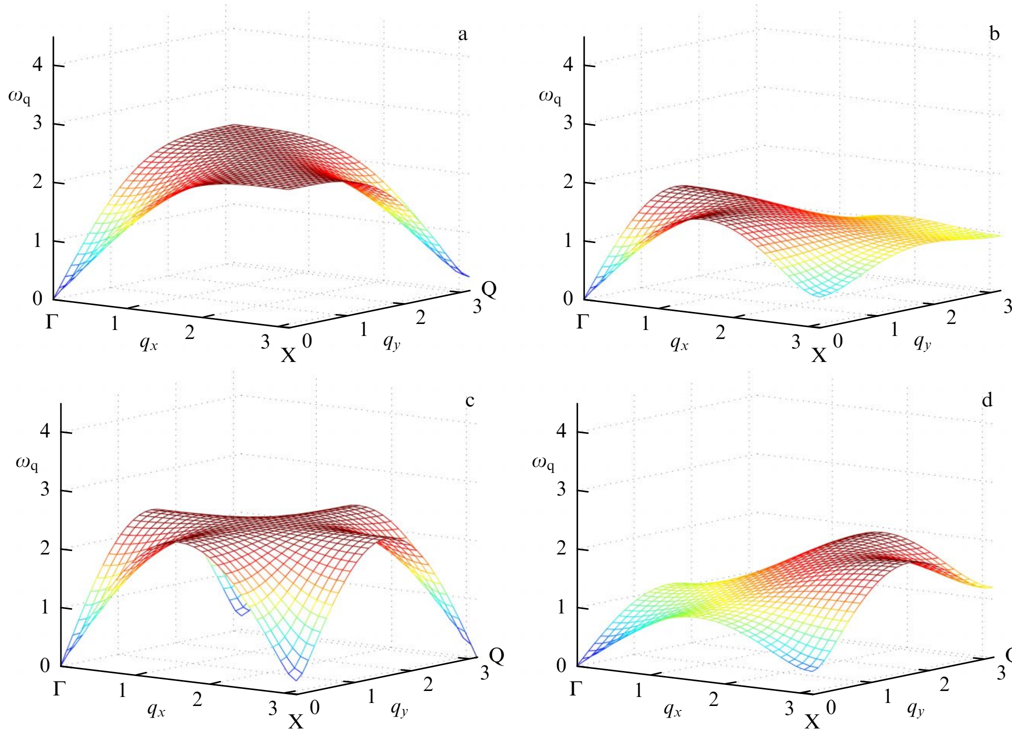

Figure 6. Spin excitation spectra at $T = 0.3$ in the upper half of the $J_1 - J_2$-circle. (a) $\varphi = 0$ corresponds to the AFM zero-temperature phase, the gap $\Delta_{\mathbf{Q}}$ is small. (b) $\varphi = \pi/4$ corresponds to the region above the spin-liquid phase, the gaps at symmetric points are comparable. (c) $\varphi = \pi/2$ corresponds to the zero-temperature stripe phase, the gaps $\Delta_{\mathbf{X}}$ are small (for $\Delta_{\mathbf{Q}}$ at $\varphi = \pi/2$, see text). (d) $\varphi = 3\pi/4$ corresponds to the region also above the spin-liquid phase, the gaps $\Delta_{\mathbf{X}}$ are somewhat larger than in the previous graph. The gap at the zero point $\Delta_{\mathbf{X}}$ is closed for any exchange and temperature. A quarter of the Brillouin zone is shown [60].

at the point $\mathbf{\Gamma} = (0, 0)$, where the gap is always closed], and the peaks of the structure factor have a finite height.

Nevertheless, short-range order retains the structure of the corresponding zero-temperature phase up to high temperatures $T \sim 1$. For example, for the region lying above the AFM phase, short-range order still preserves a checkerboard pattern ($c_g < 0$, $c_d > 0$, $c_{2g} > 0$) (see Fig. 4).

The appearance of the spin excitation spectrum also resembles that at $T = 0$, with the difference that the gaps at the corresponding symmetric points of the Brillouin zone are now nonzero.

Figure 6 shows examples of the spin spectrum at $T = 0.3$ for a wide range of exchanges along the upper semicircle. Figure 6a corresponds to $\varphi = 0$, the region of the zero-temperature AFM phase with long-range order; here, the gap at the AFM point $\Delta_{\mathbf{Q}}$ is small (recall that the gap at the zero point Δ_{Γ} is closed for any exchange and temperature). Figure 6b, $\varphi = \pi/4$, is above the spin-liquid region; the gaps at the symmetric points are comparable. Figure 6c, $\varphi = \pi/2$, is above the stripe phase with long-range order; the gaps at the stripe points $\Delta_{\mathbf{X}}$ are small (the gap $\Delta_{\mathbf{Q}}$ is always zero for the exact equality $\varphi = \pi/2$; for more details, see Footnote 12). Figure 6d, $\varphi = 3\pi/4$, is also above the spin-liquid region; the gaps at the points $\Delta_{\mathbf{X}}$ are somewhat larger than in the previous graph.

An example of the evolution of the spectrum in a local region — as φ increases from $\varphi = 0$ — is shown in Fig. 7. It can be seen that the gap at the AFM point increases, while the gaps at the stripe points decrease (although both remain nonzero); i.e., the spectrum transforms from AFM-like to stripe-like. Simultaneously, the (final) maximum of the structure factor decreases at the AFM point and increases at the stripe point.

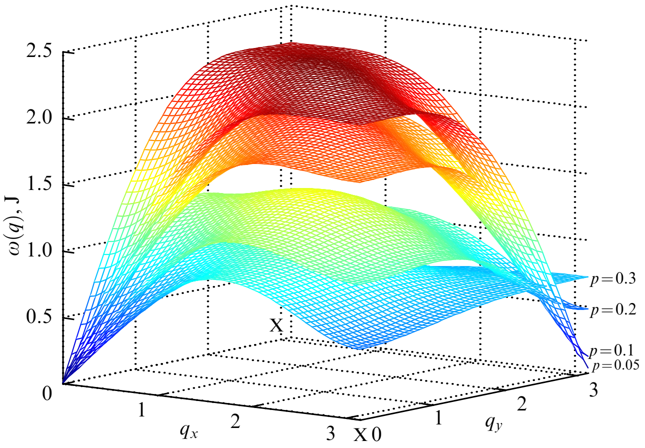

Figure 7. Evolution of the spin excitation spectrum at a finite temperature in the first quadrant of the $J_1 - J_2$ circle with increasing φ from $\varphi = 0$. In this figure from [50], the standard frustration parameter for the first quadrant is used: $p = J_2/J$, $J = J_1 + J_2$ (an increase in p corresponds to an increase in φ) and an alternative notation for the AFM point $\mathbf{M} \equiv \mathbf{Q} = (\pi, \pi)$. It is seen that with increasing p (i.e., with increasing φ), the gap at the AFM point increases, and the gaps at the stripe points $\mathbf{X}$ decrease. The nearest order transforms from the AFM- to stripe-like order. Here the temperature is $T = 0.1$ in units of $J = J_1 + J_2$, and the spectrum is in the same units.

In the lower semicircle at $T > 0$, as noted above, frustration is absent; both exchanges operate in the same direction. This leads to ‘antifrustration;’ in the third sector, $J_1 < 0, J_2 < 0$, a ‘superferromagnet’ emerges, while in the fourth sector, $J_1 > 0, J_2 < 0$, a ‘superantiferromagnet’ is realized. In these regions, at $T > 0$, the correlation length is exponentially large up to temperatures $T \sim 1$, i.e., on the order of $J = [J_1^2 + J_2^2]^{1/2}$.

Susceptibility and heat capacity. As noted at the beginning of this section, the focus is placed primarily on results concerning the spin structure. However, we will mention some other quantities calculated in the RGM.

A significant portion of the studies cited above also determined the behavior of the spin susceptibility (usually static) and heat capacity.

At $T = \text{const}$, the dependence of the static susceptibility $\chi(\mathbf{q}, \omega = 0)$ on the exchange parameters is expected: on the $J_1 - J_2$ circle, $\chi(\mathbf{q}, \omega = 0)$, calculated at a specific symmetric point $\mathbf{q}_0$ of the Brillouin zone, a maximum is observed in the region of the corresponding spin structure. The temperature behavior of the susceptibility $\chi(\mathbf{q}, \omega, T)$, at least for static susceptibility, exhibits a greater variety of regimes depending on the exchange parameters. Some studies have also analyzed the 'local spin susceptibility' $\chi_{2\mathrm{D}}(\omega, T) = \int \mathrm{d}\mathbf{q}\, \mathrm{Im}\chi(\mathbf{q}, \omega, T)$, which has a scaling property (see more details at the end of Section 9). We will avoid a full systematization of these results.

The heat capacity C_V displays a simpler behavior on the $J_1 - J_2$ circle. For any exchanges, C_V has a standard temperature dependence: $C_V \to 0$ at $T \to 0$ and a single maximum at a finite temperature, the position of which depends on the exchanges. An exception occurs in the region near the stripe ↔ FM transition, where an additional low-temperature maximum appears (first observed in [57]). In the literature, this transition is commonly attributed to frustration.

At any fixed temperature, C_V exhibits local minima in regions above ordered phases and in regions above transitions between phases. Both cases correspond to local energy extrema at $T = \text{const}$: the first case corresponds to maxima; and the second case, to minima [62].

7.2.3 Comparison with experiment and numerical methods. Numerous studies on the $J_1 - J_2$ model using the spherically symmetric approach (variations of the method are discussed in Section 8) compare the results with numerical simulations. Without going into numerous details, the agreement with the numerical results is at least satisfactory and often qualitatively good. For completeness, related models in the spherically symmetric approach are also mentioned below.

Comparisons with numerical results were carried out not only for variants of the Heisenberg model on a square lattice [23, 34, 36, 85, 86], but also for a triangular lattice [21, 23, 26], the Kagome lattice, and pyrochlore [29, 32]. Numerous comparisons with variants of a one-dimensional chain are made [8–12, 23, 86]. Finally, a similar procedure was carried out for the $t - J$ model, the most common model with a magnetic background and charge carriers (see Section 11) [53, 87, 88].

Among numerical techniques, the most common is, of course, exact diagonalization, typically in the Lanczos algorithm [8–12, 21, 23, 26, 36, 53, 86–88]. However, other methods were also used: the quantum Monte Carlo simulation [23, 34, 87], coupled cluster methods [85], and high-temperature expansions [12, 29, 32]. For one-dimensional systems, the Bethe ansatz serves as a natural benchmark [23, 86].

In summary, it can be said that the available numerical methods confirm the complete adequacy of the RGM and related approaches.

Comparison with experiment. In the early stages of theoretical development, motivated by the emergence of HTSC cuprates, comparison with experiment was essentially a mandatory requirement for papers on the topic. Almost every paper compared the fundamental characteristics of the spin excitation spectrum, fine details of the spectrum (e.g., the 'hour-glass spectrum'), the correlation length, the position of the structure factor maximum, the spin susceptibility, and other magnetic and thermodynamic characteristics with experiment. A detailed analysis of this data set, especially in the context of several different HTSC theories, is a formidable task, far beyond the scope of this review, and will not be presented here.

7.3 $J_1 - J_2 - J_3$ model

We now turn to the $J_1 - J_2 - J_3$ model.

The Hamiltonian has the form (1) with three exchanges. Recall that for a square lattice, J_1 is the exchange along the side of the square, J_2 is along the diagonal, and J_2 is along twice the side (see Fig. 1).

The calculation scheme remains the same as that described in Section 5.1, although the expressions for the Green's function become quite cumbersome (given in Section 15).

Below, the 'spherical' exchange parameterization mentioned in Section 4.1 is used

$$J_1 = \cos(\psi)\cos(\varphi),\ J_2 = \cos(\psi)\sin(\varphi),\ J_3 = \sin(\psi),$$
$$0 \leqslant \varphi \leqslant 2\pi,\ -\frac{\pi}{2} \leqslant \psi \leqslant \frac{\pi}{2},\ \sqrt{J_1^2 + J_2^2 + J_3^2} = 1\,. \quad (24)$$

This section considers the case of low but nonzero temperatures. This is quite sufficient to detect all types of emerging magnetic structures.

Figure 8 shows a section of the most interesting, fully frustrated quarter of the phase diagram, indicating the various short-range order structures. The following types of short-range order are realized: AFM, stripe, FM, and three types of quantum helices. As in the classical limit (see expressions (5)), they correspond to the positions of the

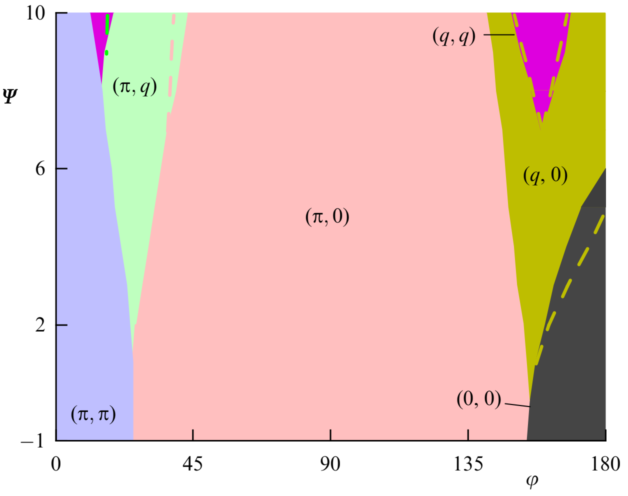

Figure 8. Phase plane regions corresponding to different short-range order structures (axis angles in degrees). The positions of the maximum structure factor are indicated. (π, π) — AFM; (π, 0) — stripe; and (0, 0) — FM. (π, q), (q, 0) and (q, q) — three types of helicoids. Solid boundaries correspond to $T = 0.4$, and dashed boundaries correspond to $T = 0.2$. At lower temperatures, the boundaries stabilize. (Data from [89, 90].)

control point (maximum of the structure factor), respectively: $\mathbf{\Gamma} = (0,0)$, $\mathbf{X} = (0,\pi), (\pi,0)$, and $\mathbf{Q} = (\pi,\pi)$. For helices, this corresponds to its motion along one side or the other of the Brillouin zone, as well as along its diagonal (helicoids $(0,q)$, $(q,0)$, and (q,q)).

Figure 8 corresponds to finite temperatures, and so only short-range order is detected everywhere. The picture remains qualitatively unchanged down to extremely low temperatures. At $T = 0$, regions of long-range order arise, separated by a spin-liquid phase. The issue of spin-liquid boundaries has been studied in detail for $J_3 = 0$ (see references in Section 7.2) and remains largely unexplored for $J_3 \neq 0$, particularly for $J_3 > 0$.

7.3.1 Frustrated helices. The most important new property that arises with the addition of J_3 is the possibility of helical spin structures, both commensurate and incommensurate. This effect is nontrivial, since helices (see, e.g., [43]), including those in 2D, are usually associated with the Dzyaloshinsky–Moriya interaction (DMI) [39–42]; references to recent works can be found in [91, 92], and for a general classification of helices, see [93]. For the realization of a DMI helix, in particular, the breaking of symmetry with respect to inversion is necessary.

In the $J_1-J_2-J_3$ model, helices arise without breaking this symmetry, without DMI interaction. The reason for their appearance here is frustration. Therefore, such helices are sometimes called frustrated, and in DMI, they are called nonfrustrated [94].

Frustrated helices — in the classical limit $S \gg 1$ — have been known since the middle of the last century. Here, the ultraquantum case $S = 1/2$ is considered in the RGM interpretation.

It is important to keep the following in mind. Quantum helical states in the RGM should not be thought of in a semiclassical manner as a lattice of spin arrows changing direction from site to site. Any spin state, including a helix, is singlet, with the average spin at a site equal to zero. The helix structure can be identified in one of three ways: by the pattern of correlators, by the position of the structure factor maximum, or by features of the spin excitation spectrum.

The first method seems obvious, but it is less intuitive. It is necessary to construct a picture of the correlators for the classical analogue of the desired quantum helix and compare it with the correlators in the quantum case (see examples in [89]). This procedure is complicated by two circumstances. First, the correlation length at $T > 0$ is finite, and the correlators decay with distance. Second, since none of the initial symmetries are broken in the RGM, the helical state is a superposition of quantum helices defined by equivalent points in the full Brillouin zone.

The second and third criteria (already mentioned in Section 7.3) are closely related. At moderate temperatures, the structure factor has a local maximum at the control point of the Brillouin zone, which determines the structure of the helix (and equivalents). At the same point, the spin excitation spectrum has a local minimum. At $T = 0$ and in the presence of long-range order, the structure factor maximum is δ-shaped, and the spin spectrum has a zero gap [the exception is the point $\mathbf{\Gamma} = (0,0)$, where the spectrum is always gapless]. Figure 9 shows an example of a structure factor maximum, in this case on the diagonal of the Brillouin zone, corresponding to a helicoid (q,q).

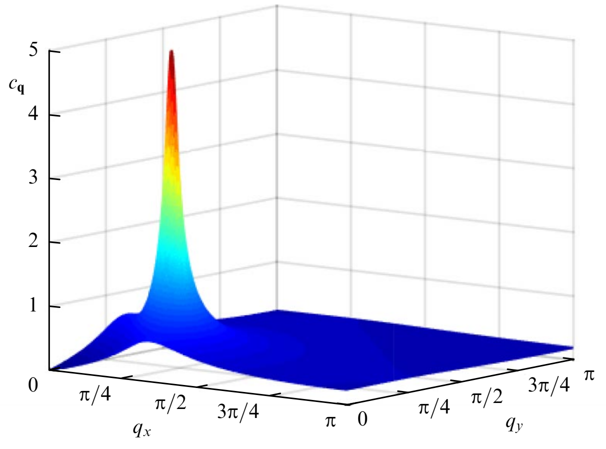

Figure 9. Example of a structure factor for a helicoid. The sharp maximum $c_{\mathbf{q}}$ on the diagonal of the Brillouin zone (helicoid (q,q)) at low temperature indicates short-range order. The peak width determines the correlation length. $T = 0.02$, $\varphi = 160°$, and $\psi = 10°$. (Data from [89].)

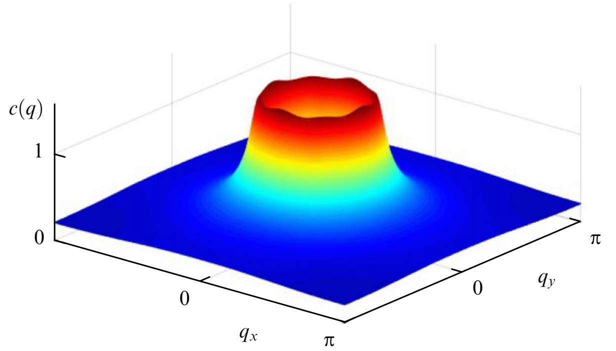

Figure 10. Structure factor with almost perfect circular symmetry. $T = 0.02$, $\varphi = 160°$, and $\psi = 10°$. The control point (q,q) is close to that determined in Fig. 9 but is shifted closer to the FM point $\mathbf{\Gamma} = (0,0)$. With this shift, the spreading of the sharp peak in Fig. 9 leads to a nearly circular structure. Unlike Fig. 9, the full Brillouin zone is shown here for clarity. (Data from [90].)

It turns out that, as in the classical limit, at $S = 1/2$, in addition to the AFM, FM, and stripe spin structures, three types of helices are realized. They correspond to the position of the $c_{\mathbf{q}}$ maximum on one of the sides or diagonals of the Brillouin zone (see Fig. 8).

The $J_1-J_2-J_3$ model exhibits another nontrivial feature that is not realized in the J_1-J_2 and J_1 models. Since the transition from one spin order motif to another occurs continuously, the most bizarre structures, in particular those with near-circular symmetry, can arise in the transition region due to their interference. An example of an isotropic helicoid is shown in Fig. 10. The structure factor acquires a nearly isotropic form as the sharp maximum in Fig. 9 spreads out, when the control point (q,q) moves along the diagonal toward the ferromagnetic point $\mathbf{\Gamma} = (0,0)$. A similar effect is observed as the control point approaches the ferromagnetic point $\mathbf{\Gamma} = (0,0)$ along the diagonal. Such spin structures can be viewed as quantum helices 'propagating in all directions.'

In the J_1-J_2 model, a truncated analog of this effect is the gradual flow of the structure factor from one symmetric point to another as it moves along the J_1-J_2 circle (see previous Section 7.3).

Susceptibility and heat capacity. Let us briefly discuss the behavior of the spin susceptibility and specific heat in the $J_1-J_2-J_3$ model.

The addition of a third exchange does not qualitatively change the behavior of C_V and $\chi(\mathbf{q}, \omega = 0)$ at all. The specific heat exhibits a standard temperature curve — a single maximum and zero asymptotics at $T \to 0$ (the exception is an additional low-temperature maximum in the region of the stripe ↔ FM transition).

The static susceptibility $\chi(\mathbf{q}, \omega = 0)$, calculated at a specific symmetric point $\mathbf{q}_0$ of the Brillouin zone, exhibits a maximum in the region of the exchange parameters corresponding to the corresponding spin structure.

An entirely nontrivial effect can be mentioned: the susceptibility $\chi(\mathbf{q}, \omega = 0)$, calculated on the diagonal of the Brillouin zone, i.e., at any point with coordinates $\mathbf{q} = (q_0, q_0)$, in addition to a maximum in the region of this point, also exhibits a smaller but comparable maximum in the region of the point $\mathbf{q} = (\pi - q_0, \pi - q_0)$. The latter corresponds to a helicoid of 'similar' structure.

7.3.2 Coexistence of two long-range orders.

In the two-dimensional quantum model $J_1-J_2-J_3$, another nontrivial effect is possible: the coexistence of two different long-range orders at $T = 0$ [95]. Simple geometric considerations already indicate this possibility. As can be seen from Fig. 11, on a square lattice, the negative third exchange J_3 favors both antiferromagnetic and stripe orders simultaneously.

In the RGM, in the quantum case $S = 1/2$, this leads to the appearance of a state with two coexisting long-range orders — antiferromagnetic and stripe — at $J_1, J_2 > 0$, and a sufficiently large absolute value of $J_3 < 0$ in a certain range of the parameter J_2/J_1 (Fig. 12).

The structure factor $c_{\mathbf{q}}$ of this state exhibits δ-shaped peaks both at the AFM point of the Brillouin zone $\mathbf{Q} = (\pi, \pi)$ and at the stripe points $\mathbf{X} = (0, \pi), (\pi, 0)$. Spin condensates of both symmetries are present (see Section 7.2 for details). The intensity of the AFM condensate decreases, while that of the stripe condensate increases, with increasing J_2/J_1 from one side of the region with two condensates to the other. The spin excitation spectrum has zero gaps at all four highly symmetric points: $\mathbf{\Gamma} = (0, 0)$, $\mathbf{X} = (0, \pi), (\pi, 0)$, and $\mathbf{Q} = (\pi, \pi)$.

Thus, the transition from the AFM phase to the stripe phase at positive and small negative J_3 occurs through the spin-liquid phase, and at large negative J_3, through a phase with two long-range orders.

In the classical limit, the described effect is impossible. This is intuitively obvious, but a rigorous proof, i.e., substituting ansatz (2) into the classical expression for the energy followed by minimization, also yields the same answer.

The coexistence of different spin orders in the RGM was already mentioned in Sections 7.2 and 7.3.1. In particular, at $T = 0$, the stripe phase is a quantum superposition of two long-range orders. The case described here differs in that two long-range orders of different symmetries coexist.

7.3.3 $J_1-J_2-J_3$ and experiment.

The above may seem like beautiful, but merely model speculation, since it is difficult to expect the exchange relation $J_3 \sim J_1, J_2$ to be realized in experiment. This can only be achieved with a suitable quantum simulator (textbook reviews [96–99] and a recent forecast review [99]).

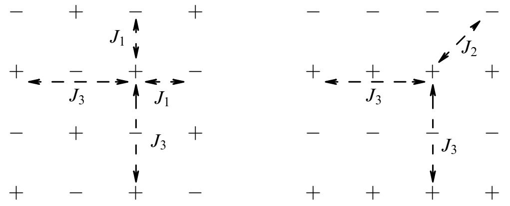

Figure 11. Negative, i.e., ferromagnetic, exchange J_3 (at twice the lattice constant) favors both antiferromagnetic and stripe phase. In the first case, AFM coupling is realized between the nearest neighbors; in the second, between the second nearest neighbors. In both cases, coupling between the third-nearest neighbors is antiferromagnetic.

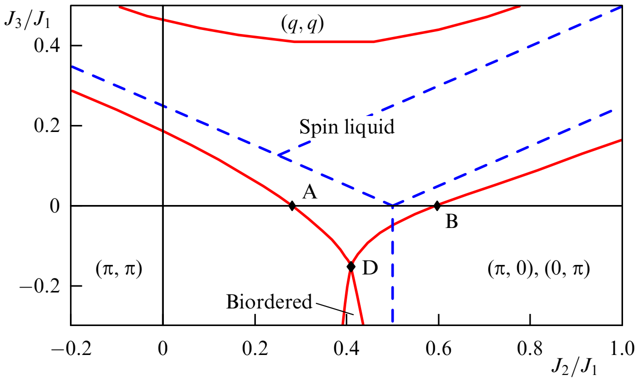

Figure 12. Section of the phase diagram of the $J_1-J_2-J_3$ model at $T = 0$; an exchange parameterization different from form (4) is used. The red lines are the boundaries of quantum phases: at the top is the diagonal helicoid $\mathbf{q} = (q, q)$, in the center is the spin liquid, at the bottom left is the AFM, at the bottom right is the long-range stripe order, and at the bottom center is the phase with two orders. The dotted lines correspond to the boundaries of classical phases: at the bottom is the AFM and stripe, and above are two helicoids. (Data from [95].)

Note that in some areas of the phase diagram, helicoids arise even at small J_3 values. This makes the experimental realization of the $J_1-J_2-J_3$ helix realistic. One possible example is (CuBr)$Sr_2Nb_3O_{10}$, a quasi-two-dimensional compound with a square lattice in the plane. A neutron experiment [100–103] reveals a peak in the structure factor at the position $(3\pi/4, 0)$, which corresponds to a commensurate spin helix. There is no symmetry breaking with respect to inversion, which makes the DMI scenario impossible.

The standard implementation of the RGM for the $J_1-J_2-J_3$ model allows one to obtain the peak position at the point $(3\pi/4, 0)$ for low temperatures at a sufficiently small J_3 ($J_1 = -0.81$, $J_2 = 0.56$, $J_3 = 0.17$) [95]. In this case, the experimentally observed heat capacity and spin susceptibility of the system are reproduced with good accuracy.

8. Relationship to other spherically symmetric approaches

In addition to the above-described approach, there exist other spherically symmetric methods that differ from the RGM. However, they are based on the same idea — description of a state with zero mean spin at a site by extracting spin-spin correlators from the Green's function. All these methods employ double-time retarded Green's functions, for which several canonical analysis algorithms are available. Essentially, each method represents an adaptation of a canonical algorithm to the constrains of spherical symmetry and zero on-site spin. All approaches, despite some mathematical differences, are conceptually close to one another, and it is often difficult to draw a strict boundary between them. Their results agree qualitatively, and often quantitatively, with high accuracy. The key dependences are essentially the same. In simplified terms, we can ascertain that the differences in the numerical results reduces to manipulating the vertex corrections.[13]

The approach described in the previous sections represents an adaptation of one of the standard algorithms: successive differentiation with respect to the 'second' time and chain closure with the extraction of spin-spin correlators. Some approaches related to the RGM are briefly described below.

8.1 Matrix projection method

In principle, the Zwanzig–Mori–Tserkovnikov projection method [104–111] is universal, in the sense that its corresponding version can be used for states with both zero and nonzero average spin at the site. A possible adaptation of the scheme to the spherically symmetric case is presented below [61]. This variant is closest to the RGM, and with some simplifications, it directly transforms into the RGM. Therefore, it is described below in somewhat greater detail.

First, we present the basic equations of the method in general form.

Let us calculate the double-time retarded Green's functions for a set of operators $\hat{A}_i$, ($i = 1-n$)

$$G_{ij} = \langle \hat{A}_i | \hat{A}_j \rangle_{\omega+\mathrm{i}\delta} = -i\int_0^\infty \mathrm{d}t\, \exp(\mathrm{i}\omega t) \langle [\hat{A}_i(t), \hat{A}_j^+] \rangle . \quad (25)$$

Here, i is not the site index, as above, but the operator number. The operators $\hat{A}_i$ form a vector $\mathbf{A} = \{\hat{A}_1 \ldots \hat{A}_n\}$.

Let us introduce matrix notation. We denote the $n \times n$ matrix of Green's functions G_{ij} by $\mathbf{G}$, the overlap matrix $K_{ij} = \langle [\hat{A}_i, \hat{A}_j^+] \rangle$ by $\mathbf{K} = \langle [\mathbf{A}, \mathbf{A}^+] \rangle$, and the frequency matrix by $\omega = \omega \mathbf{I}$, $(\mathbf{I})_{ij} = \delta_{ij}$.

We now introduce the vector $\mathbf{B} = \hat{B}_1 \ldots \hat{B}_n$ of operators $\hat{B}_i$ arising in the chain of equations for the Green's functions $\mathbf{B} = [\mathbf{A}, \hat{H}]$ ($\hat{H}$ is the Hamiltonian), as well as the energy matrix $\mathbf{\Omega} = \langle [\mathbf{B}, \mathbf{A}^+] \rangle$, determined by the commutator means $\Omega_{ij} = \langle [\hat{B}_i, \hat{A}_j^+] \rangle$.

Then it can be shown that the analog of the Dyson equation for $\mathbf{G}$ has the form

$$\mathbf{G} \times (\omega - \mathbf{K}^{-1}\mathbf{\Omega} - \mathbf{K}^{-1}\mathbf{L}^{\mathrm{irr}}) = \mathbf{K} , \quad (26)$$

where the matrix of irreducible parts is expressed as

$$\mathbf{L}^{\mathrm{irr}} = \langle \mathbf{B} | \mathbf{B}^+ \rangle - \langle \mathbf{B} | \mathbf{A}^+ \rangle \, \mathbf{G}^{-1} \langle \mathbf{A} | \mathbf{B}^+ \rangle , \quad (27)$$

and its elements have the form

$$L_{ij}^{\mathrm{irr}} = \langle \hat{B}_i | \hat{B}_j^+ \rangle - \langle \hat{B}_i | \hat{A}_s^+ \rangle (\hat{G}^{-1})_{\mathrm{st}} \langle \hat{A}_t | \hat{B}_j^+ \rangle . \quad (28)$$

We now return to the spherically symmetric approach. We introduce notations for successive commutators

$$D_{\mathbf{n}}^z = [S_{\mathbf{n}}^z, \hat{H}]; \quad W_{\mathbf{n}}^z = \big[[S_{\mathbf{n}}^z, \hat{H}], \hat{H}\big] = [D_{\mathbf{n}}^z, \hat{H}] . \quad (29)$$

Then the first two steps in the chain of equations for the Green's function (8) and (9) can be written in a compact form

$$\omega \langle S_{\mathbf{n}}^z | S_{\mathbf{m}}^z \rangle = \langle D_{\mathbf{n}}^z | S_{\mathbf{m}}^z \rangle , \quad (30)$$

$$\omega \langle D_{\mathbf{n}}^z | S_{\mathbf{m}}^z \rangle = \langle [D_{\mathbf{n}}^z, S_{\mathbf{m}}^z] \rangle + \langle W_{\mathbf{n}}^z | S_{\mathbf{m}}^z \rangle . \quad (31)$$

Here, the frequency indices are omitted for simplicity.

Next, in the standard RGM algorithm (described in Section 5), spin-spin correlation functions with vertex corrections are extracted from the three-site terms on the right-hand side of (31). The projection method implements a slightly different approach. After the Fourier transform, the system of equations (30) and (31) takes the form

$$\omega \langle S_{\mathbf{q}}^z | (S_{\mathbf{q}}^z)^+ \rangle = \langle D_{\mathbf{q}}^z | (S_{\mathbf{q}}^z)^+ \rangle , \quad (32)$$

$$\omega \langle D_{\mathbf{q}}^z | (S_{\mathbf{q}}^z)^+ \rangle = F_{\mathbf{q}} + \langle W_{\mathbf{q}}^z | (S_{\mathbf{q}}^z)^+ \rangle . \quad (33)$$

The specific expressions for $D_{\mathbf{q}}^z$, $F_{\mathbf{q}}$ and $W_{\mathbf{q}}^z$ depend on the model (J_1, $J_1 - J_2$ or $J_1 - J_2 - J_3$), and we will not present them here. In particular, $F_{\mathbf{q}}$ is the numerator of the Green's function (11). We emphasize that equations (32) and (33) are exact at this stage.

Let us now move on to implementing the projection method. We will limit ourselves to a basis of two operators; then, their choice is obvious: $\hat{A}_1 = S_{\mathbf{q}}^z$, $\hat{A}_2 = D_{\mathbf{q}}^z$. In this basis, the quantities in (26) take the form

$$\mathbf{K} = \begin{vmatrix} 0 & F_{\mathbf{q}} \\ F_{\mathbf{q}} & 0 \end{vmatrix} , \quad (34)$$

$$\mathbf{K}^{-1}\mathbf{\Omega} = \begin{vmatrix} 0 & \omega_{\mathbf{q}}^2 \\ 1 & 0 \end{vmatrix} , \quad (35)$$

where $\omega_{\mathbf{q}}^2 = F_{\mathbf{q}}^{-1} \langle W_{\mathbf{q}}^z | (D_{\mathbf{q}}^z)^+ \rangle$, and the matrix of irreducible parts is expressed as

$$\mathbf{L}^{\mathrm{irr}} = \begin{vmatrix} 0 & 0 \\ 0 & \langle W_{\mathbf{q}}^z | (W_{\mathbf{q}}^z)^+ \rangle^{\mathrm{irr}} \end{vmatrix} . \quad (36)$$

Then, the left-hand side of (26) becomes

$$(\omega - \mathbf{K}^{-1}\mathbf{\Omega} - \mathbf{K}^{-1}\mathbf{L}^{\mathrm{irr}}) = \begin{vmatrix} \omega & -\omega_{\mathbf{q}}^2 - F_{\mathbf{q}}^{-1} \langle W_{\mathbf{q}}^z | (W_{\mathbf{q}}^z)^+ \rangle^{\mathrm{irr}} \\ -1 & \omega \end{vmatrix} . \quad (37)$$

And finally, equation (26) takes the form

$$\begin{vmatrix} G_{11} & G_{12} \\ G_{21} & G_{22} \end{vmatrix} \begin{vmatrix} \omega & -\omega_{\mathbf{q}}^2 - F_{\mathbf{q}}^{-1} \langle W_{\mathbf{q}}^z | (W_{\mathbf{q}}^z)^+ \rangle^{\mathrm{irr}} \\ -1 & \omega \end{vmatrix} = \begin{vmatrix} 0 & F_{\mathbf{q}} \\ F_{\mathbf{q}} & 0 \end{vmatrix} . \quad (38)$$

The solution of the pair of equations related to the top row of the matrix $\mathbf{G}$

$$\omega G_{11} - G_{12} = 0 , \quad (39)$$

$$-G_{11} \left[(\omega_{\mathbf{q}}^2 + F_{\mathbf{q}}^{-1} \langle W_{\mathbf{q}}^z | (W_{\mathbf{q}}^z)^+ \rangle^{\mathrm{irr}}) \right] = F_{\mathbf{q}} \quad (40)$$

yields the Green's function $G_{11} = G^{zz}(\omega, \mathbf{q})$[14]

$$G_{11} = G^{zz}(\omega, \mathbf{q}) = \frac{F_{\mathbf{q}}}{\omega^2 - \left[(\omega_{\mathbf{q}}^2 + F_{\mathbf{q}}^{-1} \langle W_{\mathbf{q}}^z | (W_{\mathbf{q}}^z)^+ \rangle^{\mathrm{irr}}) \right]} . \quad (41)$$

This is the Green's function of interest.

---

[13] Since this section is devoted not to specific results, but to methods analogous to the RGM, we will mention works related not only to the square lattice, but also to other geometries.

[14] Here, for clarity, both superscripts of the Green's function G^{zz} are preserved.

Two remarks should be made here. First, in deriving relations (34)–(41), the constraints of the RGM are strictly observed, i.e., the requirements of spherical symmetry and zero mean spin at the site. And, secondly, all the indicated relations are still exact.

In expression (41), the quantity $\omega_{\mathbf{q}}$ corresponds to the mean-field spectrum of spin excitations, and taking $\langle W^z_{\mathbf{q}} | (W^z_{\mathbf{q}})^+ \rangle^{\mathrm{irr}}$ into account leads to going beyond the mean field, in particular, to the occurrence of damping.

It can be shown [61] that if some simplifications are made in the successive calculation of $\omega_{\mathbf{q}}$, then the resulting expression is reduced to the standard spectrum of the spin-field spin excitation (with vertex corrections). Attempting to go further, however, inevitably leads to the conclusion about the **q**-dependence of the vertex corrections. However, a direct determination of its form faces significant mathematical difficulties.

These difficulties can be partially overcome using a semi-phenomenological approach by assuming a physically natural **q**-dependence of the vertices (details in [61]) and taking it into account in the full self-consistency procedure. Even this simplest version significantly improves the quantitative results of the RGM.

This applies, in particular, to the zero-temperature limit in the single-exchange model, i.e., the point $J_2 = J_3 = 0$, $T = 0$, which has been studied in detail by alternative, primarily numerical, methods. Here, the basic version of the RGM, depending on the choice of vertices, provides good agreement with the numerical data either only for energy (i.e., for the first correlator) or only for the effective magnetization (for the correlator at infinity). Taking the **q**-dependence of the vertices into account eliminates this problem.

Some other methods for 'fine-tuning' the RGM are described in Section 9.

8.2 Continued fraction method and others

The continued fraction method is based on the Mori projection operator technique [108, 109] for double-time retarded Green's functions of form (7) (similar to Sections 5 and 8.1). This method has been applied within the $t-J$ model on triangular [22] and square [87, 112] lattices, as well as for various variations of the Heisenberg model on a triangular lattice ($S = 1/2$ J_1 [21], $S = 1$ $J_1 - J_2$ [24] and $S = 1$ $J_1 - J_3$ [25]).

Within this method, the spin Green's function can be represented in continued-fraction form (see, e.g., [87]):

$$G^{zz}(\omega, \mathbf{q}) = \cfrac{F_{\mathbf{q}}}{\omega - E_0 - \cfrac{V_0}{\omega - E_1 - \cfrac{V_1}{\ddots}}}\,, \tag{42}$$

where, in the general case, the elements E_i and V_i are calculated using the recursive procedure:

$$[A_n, H] = E_n A_n + A_{n+1} + V_{n-1} A_{n-1}\,, \tag{43}$$

$$E_n = \big([A_n, H], A_n^{\dagger}\big)\big(A_n, A_n^{\dagger}\big)^{-1}\,, \tag{44}$$

$$V_{n-1} = \big(A_n, A_n^{\dagger}\big)\big(A_{n-1}, A_{n-1}^{\dagger}\big)^{-1}\,. \tag{45}$$

The operators A_i form an orthogonal set satisfying the condition $(A_i, A_j^{\dagger}) \propto \delta_{ij}$, where the notation

$$(A, B) = i \int_0^{\infty} \mathrm{d}t \,\big\langle [A(t), B] \big\rangle\,. \tag{46}$$

is introduced.

For spin models, the starting point of the recursion is chosen as

$$V_{-1} = 0\,, \quad A_0 = S^z_{\mathbf{q}}\,, \quad n = 0, 1, 2, \ldots \tag{47}$$

In the cited works, further calculations are performed by terminating the fraction at the second step, i.e., choosing the approximation $V_1 = 0$. This approximation is effectively equivalent to neglecting four-site (and higher) Green's functions. The resulting three-site Green's functions of the form $S^z_{\mathbf{l}} S^+_{\mathbf{m}} S^-_{\mathbf{n}}$ are decoupled in the usual way for the RGM — by introducing vertex corrections. The method strictly satisfies the requirements of spin-correlator theory by taking into account the requirement of zero magnetization at the site:

$$\langle S^z_{\mathbf{n}} \rangle = \frac{1}{2} - \langle S^-_{\mathbf{n}} S^+_{\mathbf{n}} \rangle = 0\,. \tag{48}$$

As can readily be shown, this constraint is equivalent to the constraint condition (in particular, for $S = 1/2$ $\langle S^2_{\mathbf{n}} \rangle = 3/4$).

The system of equations for the spin correlators, together with the constraint requirement (48), is solved self-consistently. If only one vertex correction is selected, the system of equations is closed, and its solution is possible without additional conditions. However, if two vertex corrections are used, additional freedom arises: the number of variables exceeds the number of equations. In this case, additional constraints on the solution must be introduced, for example, the requirement to reproduce the results of calculations by the exact diagonalization method for the value of the correlator c_g [21].

The literature also contains references to the method of differentiating the Green's function with respect to both times and the method of formally exact solution (for general reviews, see [113, 114]), modified to take into account spherical symmetry. These approaches (not discussed in detail here) ultimately lead to similar decouplings and the same expression for the Green's function as everywhere above.

9. "Fine-tuning" of the calculations

As noted in Section 6, the RGM, although sophisticated and cumbersome, allowing many effects in low-dimensional magnets to be described, is still a mean-field approach. In its basic version, it is impossible to determine the damping of spin excitations.

This limitation can only be corrected phenomenologically [50, 54, 55, 115] (or, more accurately, semi-phenomenologically; see explanations below). One such approach was discussed above in Section 8.1. Another possible approach is described below.

Real and imaginary renormalizations are introduced into the expression for the Green's function (11), which takes the form

$$\begin{aligned} G^z(\mathbf{q}, \omega) &= \frac{F_{\mathbf{q}}}{\omega^2 - \omega^2_{\mathbf{q}} - M(\mathbf{q}, \omega)}\,, \\ M(\mathbf{q}, \omega) &= \mathrm{Re}\, M + \mathrm{i}\, \mathrm{Im}\, M\,. \end{aligned} \tag{49}$$

The form of Eqn (49) seems intuitively obvious. However, this is a formally exact expression for the Green's function $\langle S^z_{\mathbf{q}} | S^z_{-\mathbf{q}} \rangle_{\omega}$ and can be obtained using the method of irreducible Green's functions (see Section 8 for details).

Here, $M(\mathbf{q},\omega)$ is the Fourier transform of a new complex Green's function, whose analytical properties are the same as those of $G^z(\mathbf{q},\omega)$ [116]. The function $M(\mathbf{q},\omega)$ corresponds to a three-site irreducible retarded Green's function and describes the decay of a spin excitation.

Direct calculation of $M(\mathbf{q},\omega)$, even for the simplest models, presents a significant mathematical challenge, and so one must resort to a semi-phenomenological analysis.

Let us rewrite Eqn (49) in a slightly different form

$$G^z(\mathbf{q},\omega)=\frac{F_\mathbf{q}}{\omega^2-\widetilde{\omega}_\mathbf{q}^2+\mathrm{i}\omega\gamma(\mathbf{q},\omega)}\,. \tag{50}$$

In Eqn (50), $\widetilde{\omega}_\mathbf{q}^2=\omega_\mathbf{q}^2-\operatorname{Re}M_\mathbf{q}$ gives an effective renormalized spectrum of spin waves (if the dependence of $\operatorname{Re}M_\mathbf{q}$ on ω is neglected). The imaginary part of the renormalization is an odd function of ω, and Eqn (50) is written with $\operatorname{Im}M=-\omega\gamma(\mathbf{q},\omega)$, which is convenient for specific calculations (thus, $\gamma(\mathbf{q},\omega)$) is an even function of ω).

Explanatory remarks. The term 'semi-phenomenological' is used in the following sense. On the one hand, the functional form of the real and imaginary renormalizations and their coefficients are not calculated directly, but are introduced 'from the outside' and determined taking into account additional considerations and constraints. However, on the other hand, the contributions from the renormalizations are generally included in the full self-consistency procedure.

The introduction of renormalizations allows one to improve the quantitative results of the RGM and sometimes to describe effects that are in principle inaccessible with the original Green's function (11). Omitting technical details and limiting ourselves to basic references, we present two examples, both related to the J_1-J_2 model.

Width of the spin-liquid region. At $T=0$, the basic version of the RGM correctly determines the sequence of phases with and without long-range order over the entire J_1-J_2 circle (see Fig. 3).

This is also true for the first quarter of the circle: $J_1>0$, $J_2>0$. At $J_1\gg J_2$, $J_1\sim J_2$, and $J_1\ll J_2$, the RGM predicts an AFM phase with long-range order, a spin-liquid (SL) phase without long-range order, and a stripe phase with long-range order, respectively.

The AFM–SL and SL–stripe transitions on a square lattice are canonical, textbook examples of quantum phase transitions [38], and have therefore been studied in detail using various analytical and numerical methods. The transition points, and therefore the width of the spin-liquid region, are considered reliably established. The RGM with the Green's function (11) overestimates the width of this region.

However, even the simplest renormalization of the form of Eqn (50) with $\operatorname{Re}M=0$, $\gamma(\mathbf{q},\omega)=\text{const}$ at moderate values of γ returns the SL region to consensus values.

Spin susceptibility scaling. Even in the early stages of HTSC research in quasi-two-dimensional cuprates, susceptibility scaling was discovered ([117], see also the relevant section [118]).

The scaling law concerns the so-called 'local spin susceptibility' $\chi_{2\mathrm{D}}(\omega,T)$, i.e., the imaginary part of the susceptibility integrated over the quasi-momentum.

$$\chi_{2\mathrm{D}}(\omega,T)=\int\mathrm{d}\mathbf{q}\,\operatorname{Im}\chi\left(\mathbf{q},\omega,T\right). \tag{51}$$

It turns out that the dependence of $\chi_{2\mathrm{D}}$ on ω and T over a wide range of doping values is well described by the expression

$$\frac{\chi_{2\mathrm{D}}(\omega,T)}{\chi_{2\mathrm{D}}(\omega,T\to 0)}=f\left(\frac{\omega}{T}\right), \tag{52}$$

where the scaling function f is usually approximated by the arctangent of a cubic polynomial with coefficients dependent on the doping.

It is easy to show that in the basic version of the RGM, without damping of spin excitations, this effect cannot in principle be described. However, even a simple renormalization of Eqn (50), where $\operatorname{Re}M=0$ and the damping parameter depends only on temperature (and linearly), reproduces the scaling. Moreover, in this case, the problem can even be solved analytically for fixed exchange values. The actual renormalization, meanwhile, allows a more quantitatively accurate description of the experiment for $\chi_{2\mathrm{D}}$.

Note that in more complex cases, the linear dependence of γ on temperature, which necessarily follows from scaling, serves as an additional constraint when choosing renormalizations.

10. Spherically symmetric self-consistent approach and quantum entanglement

The RGM can be applied not only to the Heisenberg model in its various variants but also to more complex structures with localized spins. This includes, in particular, the spin-orbit model (spin-pseudospin, the Kugel'–Khomskii model [119, 120]).

Research on this model, proposed back in the 1970s, has recently experienced a surge in interest, which is due to two factors.

First, the orbital waves predicted by the model have finally been experimentally detected in this century [121–124].

Second, the spin-orbit model has proven to be an extremely convenient testing ground for studying multiparticle quantum entanglement [125–132]. Analytical progress in this area is nearly impossible. Obtaining a numerical result is also difficult, since it is necessary to determine the density matrix of the macroscopic system. The features of the spin-pseudospin model — a natural division into two subsystems, the mathematical identity of the spin and pseudospin operators, and the availability of high-level spin computational packages — simplify this work. However, resource consumption also limits the system size to a small one.

Analysis with the RGM, although it makes it impossible to rigorously determine the degree of entanglement, allows one to identify 'suspicious regions' and qualitatively predict expected results [133, 134]. It is even more suitable for describing the standard magnetic and thermodynamic properties of the model.

The Hamiltonian of the spin-pseudospin model has the form [119, 120]

$$\hat{H}=J\sum_{\langle\mathbf{i},\mathbf{j}\rangle}\hat{\mathbf{S}}_\mathbf{i}\hat{\mathbf{S}}_\mathbf{j}+I\sum_{\langle\mathbf{i},\mathbf{j}\rangle}\hat{\mathbf{T}}_\mathbf{i}\hat{\mathbf{T}}_\mathbf{j}+K\sum_{\langle\mathbf{i},\mathbf{j}\rangle}(\hat{\mathbf{S}}_\mathbf{i}\hat{\mathbf{S}}_\mathbf{j})(\hat{\mathbf{T}}_\mathbf{i}\hat{\mathbf{T}}_\mathbf{j})\,. \tag{53}$$

At each lattice site, the spin $S=1/2$ and pseudospin $T=1/2$ are fixed. The internal interactions in the spin and pseudospin subsystems have a Heisenberg form, and the interaction between the subsystems is the last term in Eqn (53). As in Hamiltonian (1), $\langle\mathbf{i},\,\mathbf{j}\rangle$ denotes summation over pairs of nearest neighbor sites.

Expression (53) represents the most symmetric, $SU(2) \times SU(2)$, form of the model; in other variants, the pseudospin part may be different.

Let us consider low-dimensional (1D chain and 2D square) lattices at $T > 0$. According to the Mermin–Wagner theorem [16], long-range order is impossible for uncoupled subsystems ($K = 0$). It is natural to assume that with the inclusion of intersubsystem interactions $K \neq 0$, the role of temperature and quantum fluctuations only increases, and long-range order is absent. This justifies the use of the RGM scheme.

Thus, the initial assumptions are conceptually the same as those in the Heisenberg model: the single-site mean for spin and pseudospin is zero $\langle \hat{S}_{\mathbf{i}} \rangle = \langle \hat{T}_{\mathbf{i}} \rangle = 0$, and the correlation functions $\langle \hat{S}^{\alpha}_{\mathbf{i}} \hat{S}^{\beta}_{\mathbf{j}} \rangle$, $\langle \hat{T}^{\alpha}_{\mathbf{i}} \hat{T}^{\beta}_{\mathbf{j}} \rangle$, and $\langle \hat{S}^{\alpha}_{\mathbf{i}} \hat{T}^{\beta}_{\mathbf{j}} \rangle$ are zero at $\alpha \neq \beta$ and do not depend on α at $\alpha = \beta$.

It is necessary to consider three interconnected Green's functions: spin-spin $\langle S^z_{\mathbf{q}} | S^z_{-\mathbf{q}} \rangle_{\omega}$, spin-pseudospin $\langle T^z_{\mathbf{q}} | S^z_{-\mathbf{q}} \rangle_{\omega}$, and pseudospin-pseudospin $\langle T^z_{\mathbf{q}} | T^z_{-\mathbf{q}} \rangle_{\omega}$. It can be shown [135] that the effects of the interaction of spin and orbital degrees of freedom, including entanglement [126, 136], are expressed most clearly and vividly at $J = I > 0$ and $K < 0$. At $J = I$, obviously, $\langle S^z_{\mathbf{q}} | S^z_{-\mathbf{q}} \rangle_{\omega} = \langle T^z_{\mathbf{q}} | T^z_{-\mathbf{q}} \rangle_{\omega}$, and two Green's functions remain.

However, even with these simplifications, calculations according to scheme (8)–(9) cannot be carried out, since commutation of the spin (pseudospin) operator with the last term in Eqn (53) will lead too far, and it will not be possible to close the chain of equations of motion. Nevertheless, simplifying the term of the intersubsystem interaction in terms of the mean field (with conservation of intrasite spin-pseudospin interactions, for details see [133]), one can obtain a closed system, the solution of which leads to nontrivial results.

Taking into account the interaction of subsystems, the spin-spin Green's function $G^z(\mathbf{q}, \omega) = \langle S^z_{\mathbf{q}} | S^z_{-\mathbf{q}} \rangle_{\omega}$ and the spin-pseudospin Green's function take the form

$$G^z(\mathbf{q}, \omega) = \langle S^z_{\mathbf{q}} | S^z_{-\mathbf{q}} \rangle_{\omega} = \frac{F_{\mathrm{ac}}(\mathbf{q})}{\omega^2 - \omega^2_{\mathrm{ac}}(\mathbf{q})} + \frac{F_{\mathrm{opt}}(\mathbf{q})}{\omega^2 - \omega^2_{\mathrm{opt}}(\mathbf{q})} , \quad (54)$$

$$R^z(\mathbf{q}, \omega) = \langle T^z_{\mathbf{q}} | S^z_{-\mathbf{q}} \rangle_{\omega} = \frac{F_{\mathrm{ac}}(\mathbf{q})}{\omega^2 - \omega^2_{\mathrm{ac}}(\mathbf{q})} - \frac{F_{\mathrm{opt}}(\mathbf{q})}{\omega^2 - \omega^2_{\mathrm{opt}}(\mathbf{q})} . \quad (55)$$

Specific expressions for the numerators and spectra in (54) and (55), which are not essential for the further presentation, can be found in [133].

The main results of the RGM for low-dimensional spin-pseudospin models are as follows. At a fixed temperature $T > 0$, with an increase in the modulus of the intersubsystem interaction $|K|$ (recall that $K < 0$), starting from a certain boundary value K_{c}, nonzero spin-pseudospin correlators appear — intrasite $m_0 = \langle S^z_{\mathbf{i}} T^z_{\mathbf{i}} \rangle$ and intersite $m_g = \langle S^z_{\mathbf{i}} T^z_{\mathbf{ig}} \rangle$ — for 2D (Fig. 13a).

The boundaries of the regions with zero and nonzero spin-pseudospin correlators in 1D and 2D are shown in Fig. 13b. Noteworthy is the counterintuitive behavior of the boundary in the one-dimensional case: in a certain range of intersubsystem interactions, a reversible transition is observed with increasing temperature.

Simultaneously with the appearance of intersubsystem correlators, the excitation spectrum splits into acoustic and optical branches (Fig. 14a) (2D). For small $|K|$, the splitting is noticeable mainly at the symmetric points of the Brillouin zone $\mathbf{\Gamma}$ and $\mathbf{Q}$. For large $|K|$, the upper sections of the spectrum branches form an almost dispersion-free region (see Fig. 14a).

At the transition point, the heat capacity of the system also experiences a jump. The greater the jump, the greater the critical value of $|K|$ (Fig. 14b) (2D). Both susceptibilities undergo simultaneous jumps: spin-spin $\chi_{\mathrm{ss}}(\mathbf{q}, \omega) = -G^z(\mathbf{q}, \omega)$ and spin-pseudospin $\chi_{\mathrm{st}}(\mathbf{q}, \omega) = -R^z(\mathbf{q}, \omega)$.

The indicators mentioned above can apparently be considered entanglement witnesses, although the theory of entanglement witnesses in condensed matter is still far from complete (see recent review [137]).

With an exact numerical solution of the problem for a small one-dimensional chain [131, 132], the conclusions obtained in the RGM, including those with respect to intersubsystem entanglement, are confirmed. In 2D, the available computational resources, even with a minimally reasonable number of particles, do not allow the evolution of entanglement to be determined.

Concluding remark. The spin-pseudospin model for a square lattice is qualitatively similar to the Heisenberg model for two interacting planes. Spins are localized on one plane, and pseudospins are localized on the other. However,

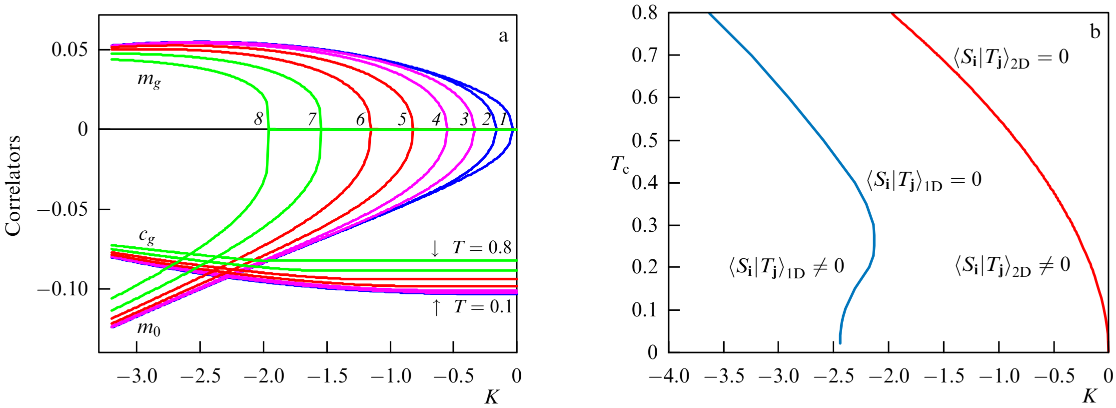

Figure 13. (a) 2D lattice. Spin–spin correlator c_g at the nearest neighbors and spin-pseudospin correlators (intrasite m_0 and intersite m_g) as functions of temperature and intersubsystem exchange K. The curves forming the 'platypus nose' are m_0 ($m_0 < 0$) and m_g ($m_g > 0$). The numbers *1*–*8* number the temperature: *1* — $T = 0.1$, *2* — $T = 0.2$, etc. The lower curves are c_g (the boundary values of T are indicated). (b) Phase diagram of the model for 1D and 2D. The boundaries of the regions with zero and nonzero spin-pseudospin correlators m_0 and m_g are shown (i.e., in the figure, $\mathbf{j} = \mathbf{i}, \mathbf{i} + \mathbf{g}$). The features of the one-dimensional case are noteworthy (see text). (Data from [133, 134].)

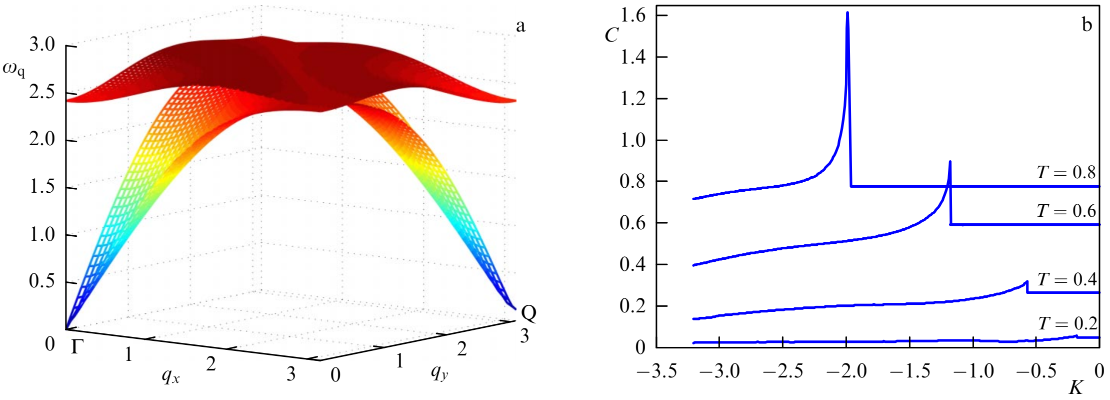

Figure 14. (a) 2D lattice. Spectra of elementary excitations $\omega_{\rm ac}(\mathbf{q})$ and $\omega_{\rm opt}(\mathbf{q})$ at $T = 0.3$ and strong splitting $K = -3.0$. The upper sections of the spectrum branches form a nearly dispersionless region. A quarter of the full Brillouin zone is shown. (b) 2D lattice. Dependence of the heat capacity at a fixed temperature on the magnitude of the intersubsystem interaction K. The horizontal sections correspond to zero values of the spin-pseudospin correlators. (Data from [133, 134].)

the interaction between them is not of the Heisenberg type, but has a more complex nature (the last term in Eqn (53)). Nevertheless, some effects in these two models are similar (see Section 12).

11. Doping models and spin polaron

During the quarter-century 'struggle for a true theory of HTSC,' many scenarios for nonphonon pairing have been proposed. A detailed description of these scenarios is a Herculean task (a brief recent review with an extensive list of references can be found in [138]). Here, we will briefly discuss only one aspect of the issue relevant to the subject of this paper, namely, the concept of the spin polaron and spin-polaron pairing (earlier reviews can be found in [139–141], a recent review with numerous references can be found in [142]; see also the relevant section of the comprehensive book on HTSC [118]).

Thus, let us consider a theoretical model in which there is a magnetic background and charge carriers strongly interact with it. This could be the $p-d$ model [142], the Kondo lattice [139, 140], various variants of the Hubbard model [143–147], the basic $t-J$ model and its variants [22, 31, 87, 88, 112, 148–151], and others. The $t-J$ model is the most frequently discussed model in the literature.

A charge carrier perturbs the AFM background, thereby increasing the energy (the effect was considered as far back as the 1960s [152]). This is easier to demonstrate with a hole as an example. Imagine a chessboard with one square removed. As the resulting hole moves along the board, the chessboard order is obviously disrupted, and the number of adjacent squares of the same color increases (for FM, such an analysis is obviously meaningless).

Of course, in advanced models, the picture is much more complex; moreover, the so-called Tragman loops [15] weaken the presented arguments [153]. However, the basic idea remains the same: a carrier moving above an AFM background significantly distorts it. The carrier plus the background perturbation form a 'good' quasiparticle — a spin polaron.

The idea of spin-polaron pairing, implemented in a wide variety of models and using numerous theoretical methods, is also fundamentally simple. Two polarons located close to each other will introduce a smaller perturbation into the magnetic background than when they are far apart. This effect can overcome the Coulomb repulsion (unlike Bardeen–Cooper–Schrieffer theory, the pair in this case is local). We emphasize once again that the above is only an extremely simplified, primitivized description.

The properties of a spin-polaron system depend on the bare spectrum of carriers, the type of their interaction with the background, and — important for this work — the structure of the magnetic subsystem. It is clear that a charge carrier living on a checkboard, Neél AFM background and the same carrier living on a singlet state with strong AFM correlations form significantly different polarons.

And here we encounter a new field of application of the RGM and similar methods. The studies mentioned above specifically use a spherically symmetric approach for the spin subsystem.

Within the framework of a rough classification, we can identify three algorithms on which these studies are based.

The *first algorithm* is the most complex (see, for example, [87, 142]). Expressions are written for both conventional charge and spin Green's functions (in some models, these may be Green's functions in Hubbard operators). Then, using some approach (always approximate), these Green's functions are calculated taking into account the interaction of the subsystems and the constraints imposed on the spin subsystem by the spherically symmetric approach. The result is a rather cumbersome system of self-consistent equations, solved numerically.

The *second algorithm* is as follows (see, for example, [139–141]). Only the charge subsystem is considered in detail, but with its interaction with the spin subsystem taken into account. This requires the use of spin-spin correlators. The latter are borrowed from calculations for the undoped but frustrated J_1-J_2 model. The connecting bridge is the assumption of an analogy between (small) doping in free-carrier models and frustration in the purely spin model. This idea is physically natural: a moving hole destroys magnetic order, and the same happens with increasing frustration in the spin model. Moreover, it is based on the long-discovered similarity in the behavior of spin correlators depending on doping and frustration [154]. Although this assumption has not been rigorously proven, it is considered sufficiently justified.

---

[15] After several traverses of the square, the hole moves diagonally, leaving behind an unperturbed magnetic configuration.

And finally, the *third algorithm* is as follows (see, for example, [147, 150]). It is similar to the second in that only the most essential elements of the spin problem are retained. The degree of mathematical detail in these most essential elements may vary, but the underlying principle is always a simple physical idea. At $T > 0$, unlike the two-sublattice antiferromagnetic state, in the singlet state with AFM correlations, the gap at the point $\mathbf{Q} = (\pi, \pi)$ of the Brillouin zone is open, and, accordingly, the AFM correlation length is finite.

Note that the above-cited references are not intended to be exhaustive, but merely serve as illustrations of the use of spherically symmetric approaches in the spin polaron concept.

12. Transition to 3D

In principle, the RGM provides a reasonable description of the three-dimensional case for both the J_1 [155] and $J_1 - J_2$ [156] models. However, for obvious reasons, this approach has not been further developed — the Mermin–Wagner theorem does not impose limitations in 3D, and standard methods are simpler and more convenient.

In the RGM, the transition from the two-dimensional to the three-dimensional case, i.e., from a square lattice to a cubic one, is of interest. In this case, it is more correct to speak of a transition to a stack of square lattices.

The first step in this direction was made in [15, 50], where two interacting planes were considered. The Hamiltonian of such a problem has the form of Eqn (56) given below for the case $n = 1, 2$.

In [15, 50], the stated goal was to quantitatively describe neutron experiments for HTSC cuprates with two closely spaced magnetic planes. Therefore, a detailed presentation of its results in the context of this review does not seem necessary. We will, however, mention one important, albeit intuitively obvious, result: when interplane interaction is included, the spin excitation spectrum splits into optical and acoustic branches. Qualitatively, this effect is similar to that observed in the spin-pseudospin model (Section 10). Of course, there is no quantitative agreement, because of the different types of interplane interaction.

The 2D → 3D transition was studied in detail in [14], where a three-dimensional stack of planar square lattices with controlled interactions was considered. In each plane, the first and second nearest neighbor AFM exchanges are taken into account; i.e., frustration is present.

Thus, the Hamiltonian of the model has the form

$$\hat{H}=\sum_n\left(J_1\sum_{\langle \mathbf{i},\mathbf{j}\rangle}\hat{\mathbf{S}}_{\mathbf{i},n}\hat{\mathbf{S}}_{\mathbf{j},n}+J_2\sum_{[\mathbf{i},\mathbf{j}]}\hat{\mathbf{S}}_{\mathbf{i},n}\hat{\mathbf{S}}_{\mathbf{j},n}\right)+J_\perp\sum_{\mathbf{i},n}\hat{\mathbf{S}}_{\mathbf{i},n}\hat{\mathbf{S}}_{\mathbf{j},n+1}\,. \tag{56}$$

Here, the subscript n numbers the different square planes. In each plane, as in the base Hamiltonian (1), $\langle \mathbf{i},\mathbf{j}\rangle$ denotes the summation over pairs of nearest neighbor sites, and $[\mathbf{i},\mathbf{j}]$ denotes the summation over pairs of next-nearest neighbors. The exchange $J_\perp$ is the interplanar interaction. We consider the first quarter of the $J_1 - J_2$ circle (see Fig. 3); i.e., the first and second exchanges are antiferromagnetic: $J_1 > 0$ (hereinafter, $J_1 = 1$) and $J_2 > 0$. The interlayer exchange $J_\perp$ is also assumed to be nonnegative, $J_\perp \geqslant 0$.

For such parameters on one plane, i.e., at $J_\perp = 0$, a spin-liquid phase without long-range order is realized at $T = 0$ in the region $J_2 \simeq 1/2$. On the side of small $J_2 < 1/2$, it borders on the AFM phase, and on the side of large $J_2 > 1/2$, it boarders on the stripe phase.[16] In a purely three-dimensional situation, the spin-liquid phase is absent. Therefore, the disappearance of the spin-liquid region with increasing $J_\perp$ serves as a natural criterion for 'true three-dimensionality'.

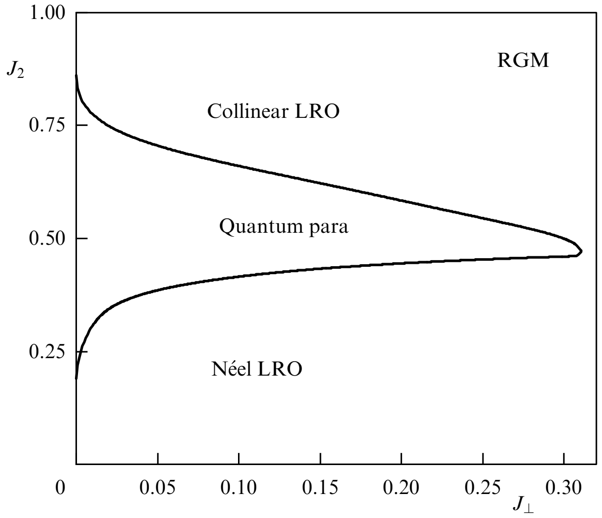

Figure 15. Phase diagram for a stack of square planes in the $J_\perp$, J_2 ($J_1 = 1$) from [14]. Here, Neél LRO is the AFM phase, quantum para is the spin liquid, and collinear LRO is the stripe phase. The RGM label in the upper right corner indicates the calculation method. For $J_\perp \geqslant 0.3J_1$, no spin liquid remains. (Data from [14].)

Omitting the technical details that make it possible to implement a spherically symmetric approach for a stack of square lattices (including the algorithm for determining vertex corrections), Fig. 15 presents the most significant result of paper [14]. One can see from the figure that with increasing $J_\perp$, the width of the spin-liquid region decreases (first rapidly, then somewhat more slowly) and at $J_\perp \sim 0.3J_1$, no spin liquid remains.

Thus, even with a sufficiently weak interaction between the planes, the effect characteristic of a purely two-dimensional system completely disappears.

13. Effect of anisotropy

The use of the RGM is not limited to the study of the isotropic Heisenberg Hamiltonian; it also allows for the consideration of various types of anisotropy. However, it should be acknowledged that the influence of anisotropy has not yet been fully studied. Below, we discuss the main results concerning some anisotropic contributions to Hamiltonian (1).

13.1 Magnetic field

In the J_1 model within the RGM, the influence of the magnetic field $\hat{\mathcal{H}} = h\sum_{\mathbf{i}} \hat{S}_{\mathbf{i}}^z$ is taken into account for both the FM [34, 86] and AFM [157] cases.

In the presence of a magnetic field, the condition for the equality of the three correlators is clearly violated and becomes $\langle S_{\mathbf{n}}^x S_{\mathbf{n+r}}^x\rangle = \langle S_{\mathbf{n}}^y S_{\mathbf{n+r}}^y\rangle \neq \langle S_{\mathbf{n}}^z S_{\mathbf{n+r}}^z\rangle$.

This results in the appearance of two different Green's functions G^{zz} and $G^{xx} = G^{yy}$ and, accordingly, increases the number of vertex corrections.

---

[16] Recall that $J_2 = 1/2$ is the AFM — stripe transition point in the classical limit.

After the standard RGM separation of correlators, the Green's functions take the form

$$G^{xx}_{\mathbf{q}}(\omega) = \frac{F^{xx}_{1\mathbf{q}}}{\omega - \omega^{+}_{\mathbf{q}}(h)} + \frac{F^{xx}_{2\mathbf{q}}}{\omega - \omega^{-}_{\mathbf{q}}(h)} \,, \tag{57}$$

$$G^{zz}_{\mathbf{q}}(\omega) = \frac{F^{zz}_{\mathbf{q}}}{\omega^2 - (\omega^z_{\mathbf{q}})^2} \,. \tag{58}$$

Explicit expressions for the numerators of the Green's functions and the spin excitation spectra are given in [34, 86, 157]. The magnetic field completely removes the degeneracy of the spin excitation branches, forming three branches: one branch, $\omega^z_{\mathbf{q}}$, depends on the magnetic field indirectly, through correlators renormalized with the magnetic field, while the other two, $\omega^{+}_{\mathbf{q}}(h)$ and $\omega^{-}_{\mathbf{q}}(h)$, depend explicitly on the field. Evidence for such a splitting is observed in a neutron experiment [158].

In the FM case, for the 2D and 1D models, spin $S = 1/2$, $S \geqslant 1$, the dependences of thermodynamic quantities (magnetization, magnetic susceptibility, and specific heat) on magnetic field and temperature were obtained [34, 86]. Power laws were found for the position and height of the maximum of magnetic susceptibility, and the presence of two maxima in the temperature dependence of the heat capacity was shown for $S = 1/2$ and $S = 1$; for $S > 1$, as in 2D, the maximum is one. The results are consistent with calculations by the exact diagonalization method [159] and the quantum Monte Carlo simulations [34].

13.2 Single-ion anisotropy

Single-ion anisotropy (the addition to the Hamiltonian $\hat{H}_{\mathrm{D}} = D\sum_{\mathbf{i}}(\hat{S}^z_{\mathbf{i}})^2$, where D is the single-ion anisotropy constant) was studied within the framework of the single-ion anisotropy model [36] for the 1D ferromagnetic case.

For the calculations, a version [160, 161] of the matrix projection method described in Section 8.1 was used in the two-operator basis $\mathbf{A}^{\nu} = (\hat{S}^{\nu}_{\mathbf{q}}, i\dot{\hat{S}}^{\nu}_{\mathbf{q}})(\nu = +, z)$. When closing the chains of equations for the Green's functions, four vertex corrections appear in the second differentiation step.

The spin excitation spectrum splits into two branches: one dependent on the anisotropy parameter $\omega^{+-}_{\mathbf{q}}(D)$ and $\omega^{zz}_{\mathbf{q}}$ one dependent on D indirectly through correlators.

The results for the thermodynamic properties (longitudinal and transverse susceptibilities, specific heat capacity) over a wide temperature range are consistent with the exact diagonalization data for finite chains. Note that the temperature dependence of the heat capacity exhibits two maxima if the ratio of the anisotropy parameter D to the exchange interaction J_1 exceeds the characteristic value $D/J_1 > 7.4$, and only one maximum at $D/J_1 < 7.4$.

13.3 Exotic anisotropies: tetragonal lattice and the compass model

The successful application of the RGM is not limited to two-dimensional systems and classical problems related to magnetic fields and single-ion anisotropy. For example, in [162], this method was used to describe the magnetism of iron pnictides, which have a three-dimensional tetragonal crystal lattice. In [162], the Heisenberg Hamiltonian on a tetragonal lattice was studied

$$\hat{H} = \frac{1}{2}\sum_{i,j} J_{ij}\,\mathbf{S}_i\,\mathbf{S}_j \,, \tag{59}$$

$$J_{ij} = J_x \delta_{\mathbf{R}_j,\,\mathbf{R}_i \pm \mathbf{a}_x} + J_y \delta_{\mathbf{R}_j,\,\mathbf{R}_i \pm \mathbf{a}_y} + J_z \delta_{\mathbf{R}_j,\,\mathbf{R}_i \pm \mathbf{a}_z} + J_2 \delta_{\mathbf{R}_j,\,\mathbf{R}_i \pm \mathbf{d}_{xy}} \,, \tag{60}$$

where J_x, J_y, and J_z are the exchange interactions between nearest neighbors along the corresponding directions, and J_2 is the exchange interaction between the second-nearest neighbors in the xy plane.

As a result, the two-spin correlation functions, the spin excitation spectrum, the Neél temperature, and the magnetization were self-consistently calculated for model (59)–(60) as functions of temperature and spin. In this study, the temperature dependence of the static magnetic susceptibility was obtained, including a linear increase over a wide temperature range, which is in good agreement with experimental data from inelastic neutron scattering. This effect is explained by the presence of strong antiferromagnetic short-range order in the xy plane. However, it was found that model (59)–(60), which takes into account interplane interactions based on neutron scattering data, cannot correctly describe antiferromagnetic long-range order in iron pnictides: the calculated Neél temperatures were approximately five times higher than the measured ones. For a more accurate description, the model must be extended to account for the interaction of localized spins and free electrons.

Another example of the application of the spherically symmetric approach to models with pronounced anisotropy is presented in the study of the compass model [163] on a square lattice [164]. This is a Heisenberg-type model, in which the exchanges along the x axis are not equal to the exchanges along the y axis. In [164], the thermodynamic characteristics of a two-dimensional antiferromagnetic Heisenberg model with compass interaction were calculated, and the dependence of the Neél temperature on the exchange parameters of the model was investigated. It was found that the Neél temperature remains finite even for symmetric interaction in the compass model. Furthermore, the influence of short-range magnetic order on the temperature dependences of static magnetic susceptibilities was explained.

14. Conclusions

The spherically symmetric self-consistent approach, which emerged half a century ago and received a significant boost in the 1990s, remains a fully functional method for studying low-dimensional spin and doped models while accurately accounting for theorem-based constraints.

This in no way contradicts the use of alternative analytical approaches: spin-wave, auxiliary bosons or fermions, and other approaches. Depending on the conditions of a particular problem, any of them may prove more effective.

Acknowledgments. The authors thank K.I. Kugel', P.A. Alekseev, R.O. Kuzyan, and A.M. Belemuk for helpful comments and detailed discussions.

15. Appendix. Green's function and spectrum in the spherically symmetric self-consistent approach

In the standard version of the RGM — the closure of the chain of equations of motion at the second step — the Fourier transform of the spin-spin Green's function has the form

$$G^z(\mathbf{q}, \omega) = \frac{F_{\mathbf{q}}}{\omega^2 - \omega^2_{\mathbf{q}}} \,. \tag{61}$$

In the $J_1 - J_2 - J_3$ model, the expressions for the numerator $F_{\mathbf{q}}$ and for the spin excitation spectrum $\omega_{\mathbf{q}}$ include the spin-spin correlation functions $c_{|\mathbf{r}|} = \langle S^z_{\mathbf{n}} S^z_{\mathbf{n}+\mathbf{r}} \rangle$ on the first three and the first eight coordination spheres, respectively,

$$F_{\mathbf{q}} = 8 \sum_{\mathbf{r} \in \{\mathbf{g}, \mathbf{d}, 2\mathbf{g}\}} J_{\mathbf{r}} (\gamma_{\mathbf{r}} - 1) c_{\mathbf{r}} \,, \tag{62}$$

$$\omega_{\mathbf{q}}^2 = 2 \sum_{i=1}^{12} \Gamma_i K_i \,, \tag{63}$$

where $\mathbf{g}$, $\mathbf{d}$ and $2\mathbf{g}$ are the vectors of the first, second, and third nearest neighbors; J_g, J_d, and J_{2g} are J_1, J_2, and J_3, respectively; $\gamma_g = 1/2\,(\cos(q_x) + \cos(q_y))$, $\gamma_d = \cos(q_x)\cos(q_y)$, $\gamma_{2g} = 1/2(\cos(2q_x) + \cos(2q_y))$.

The lattice sums K_i included in the expression for the spectrum $\omega_{\mathbf{q}}$ (63) have the form:

$$\begin{aligned}
K_1 &= J_1 J_2 K_{gd} + J_1 J_3 K_{g,\,2g} \\
&\quad + J_1^2 (z_g (z_g - 1) \tilde{c}_g + z_g c_0 + K_{gg}) \,; \\
K_2 &= J_2 J_1 K_{dg} + J_2 J_3 K_{d,\,2g} \\
&\quad + J_2^2 (z_d (z_d - 1) \tilde{c}_d + z_d c_0 + K_{dd}) \,; \\
K_3 &= -J_1^2 z_g^2 \tilde{c}_g \,; \quad K_4 = -J_2^2 z_d^2 \tilde{c}_d \,; \\
K_5 &= -J_1 J_2 z_g z_d \tilde{c}_g \,; \quad K_6 = -J_1 J_2 z_g z_d \tilde{c}_d \,; \\
K_7 &= J_3 J_1 K_{2g,\,g} + J_3 J_2 K_{2g,\,d} \\
&\quad + J_3^2 (z_{2g} (z_{2g} - 1) \tilde{c}_{2g} + z_{2g} c_0 + K_{2g,2g}) \,; \\
K_8 &= -J_3^2 z_{2g}^2 \tilde{c}_{2g} \,; \quad K_9 = -J_1 J_3 z_g z_{2g} \tilde{c}_g \,; \\
K_{10} &= -J_3 J_1 z_{2g} z_g \tilde{c}_d \,; \quad K_{11} = -J_2 J_3 z_d z_{2g} \tilde{c}_d \,; \\
K_{12} &= -J_3 J_2 z_{2g} z_d \tilde{c}_{2g} \,;
\end{aligned} \tag{64}$$

here,

$$K_{r_1, r_2} = \sum_{\mathbf{r}_1, \mathbf{r}_2, \mathbf{r}_1 \neq -\mathbf{r}_2} \tilde{c}_{\mathbf{r}_1 + \mathbf{r}_2}, \mathbf{r}_1, \mathbf{r}_2 \in \{\mathbf{g}, \mathbf{d}, 2\mathbf{g}\} \,. \tag{65}$$

The dependence of the spectrum $\omega_{\mathbf{q}}$ on the quasi-momentum is determined by the factors Γ_i

$$\begin{aligned}
&\Gamma_1 = 1 - \gamma_g ; && \Gamma_2 = 1 - \gamma_d \,; \\
&\Gamma_3 = 1 - \gamma_g^2 ; && \Gamma_4 = 1 - \gamma_d^2 \,; \\
&\Gamma_5 = (1 - \gamma_g) \gamma_d \,; && \Gamma_6 = (1 - \gamma_d) \gamma_g \,; \\
&\Gamma_7 = 1 - \gamma_{2g} \,; && \Gamma_8 = 1 - \gamma_{2g}^2 \,; \\
&\Gamma_9 = (1 - \gamma_g) \gamma_{2g} ; && \Gamma_{10} = (1 - \gamma_{2g}) \gamma_g \,; \\
&\Gamma_{11} = (1 - \gamma_d) \gamma_{2g} \,; && \Gamma_{12} = (1 - \gamma_{2g}) \gamma_d \,.
\end{aligned} \tag{66}$$

In (62) and (66), $\gamma_n = (1/z_n) \sum_i \exp(\mathrm{i}\mathbf{q}\mathbf{n}_i)$, where the sum is taken over the z_n sites of the corresponding coordination sphere. For a 2D square lattice, $z_g = z_d = z_{2g} = 4$. In (64) and (65), $\tilde{c}_r$ corresponds to the correlators c_r renormalized by the vertex corrections α_r, i.e., $\tilde{c}_r = \alpha_r c_r$. Note that the RGM also uses an alternative nomenclature for the grouping of the term in (63) (see, for example, [57, 58]).

The results for the $J_1 - J_2$ and J_1 models are obtained from the above by setting the corresponding terms to zero.

References

1. Kondo J, Yamaji K *Prog. Theor. Phys.* **47** 807 (1972)
2. Tyablikov S V *Metody Kvantovoi Teorii Magnetizma* (Methods in the Quantum Theory of Magnetism) 2nd ed., rev. and enlarg. ed. (Moscow: Nauka, 1975); Translated into English of the 1st Russian ed.: Tyablikov S V *Methods in the Quantum Theory of Magnetism* (New York: Plenum Press, 1967) DOI:10.1007/978-1-4899-7182-1
3. Callen H B *Phys. Rev.* **130** 890 (1963)
4. Shimahara H, Takada S *J. Phys. Soc. Jpn.* **60** 2394 (1991)
5. Barabanov A F, Starykh O A *J. Phys. Soc. Jpn.* **61** 704 (1992)
6. Barabanov A F, Beresovsky V M *J. Phys. Soc. Jpn.* **63** 3974 (1994)
7. Barabanov A F, Berezovskii V M *J. Exp. Theor. Phys.* **79** 627 (1994); *Zh. Eksp. Teor. Fiz.* **106** 1156 (1994)
8. Härtel M et al. *Phys. Rev. B* **78** 174412 (2008)
9. Richter J et al. *J. Phys. Conf. Ser.* **145** 012064 (2009)
10. Härtel M et al. *Phys. Rev. B* **84** 104411 (2011)
11. Hutak T et al. *Eur. Phys. J. B* **95** 93 (2022)
12. Hutak T et al. *Eur. Phys. J. B* **96** 50 (2023)
13. Schmalfuß D, Richter J, Ihle D *Phys. Rev. B* **72** 224405 (2005)
14. Schmalfuß D et al. *Phys. Rev. Lett.* **97** 157201 (2006)
15. Kozlov N A, Barabanov A F *JETP Lett.* **85** 544 (2007); *Pis'ma Zh. Eksp. Teor. Fiz.* **85** 673 (2007)
16. Mermin N D, Wagner H *Phys. Rev. Lett.* **17** 1133 (1966)
17. Marshall W *Proc. R. Soc. London A* **232** 48 (1997)
18. Starykh O A *Rep. Prog. Phys.* **78** 052502 (2015)
19. Zhou Y, Kanoda K, Ng T-K *Rev. Mod. Phys.* **89** 025003 (2017)
20. Markina M M et al. *Phys. Usp.* **64** 344 (2021); *Usp. Fiz. Nauk* **191** 358 (2021)
21. Rubin P, Sherman A *Phys. Lett. A* **334** 312 (2005)
22. Rubin P, Sherman A, Schreiber M *Phys. Lett. A* **372** 5229 (2008)
23. Antsygina T N et al. *Phys. Rev. B* **77** 024407 (2008)
24. Rubin P, Sherman A, Schreiber M *Phys. Lett. A* **374** 3567 (2010)
25. Rubin P, Sherman A, Schreiber M *Phys. Lett. A* **376** 1062 (2012) DOI:10.1016/j.physleta.2012.01.045
26. Rubin P, Sherman A *J. Phys. Conf. Ser.* **833** 012019 (2017) DOI:10.1088/1742-6596/833/1/012019
27. Yu W, Feng S *Eur. Phys. J. B* **13** 265 (2000)
28. Bernhard B H, Canals B, Lacroix C *Phys. Rev. B* **66** 104424 (2002)
29. Müller P, Zander A, Richter J *Phys. Rev. B* **98** 024414 (2018)
30. Vladimirov A A, Ihle D, Plakida N M *Eur. Phys. J. B* **90** 48 (2017)
31. Vladimirov A A, Ihle D, Plakida N M *Eur. Phys. J. B* **91** 195 (2018)
32. Müller P et al. *Phys. Rev. B* **96** 174419 (2017)
33. Müller P et al. *Phys. Rev. B* **100** 024424 (2019)
34. Junger I J et al. *Phys. Rev. B* **77** 174411 (2008)
35. Suzuki F, Shimata N, Ishii C *J. Phys. Soc. Jpn.* **63** 1539 (1994)
36. Junger I J, Ihle D, Richter J *Phys. Rev. B* **72** 064454 (2005)
37. Auerbach A, Arovas D P "Schwinger bosons approaches to quantum antiferromagnetism," in *Introduction to Frustrated Magnetism. Materials, Experiments, Theory* (Springer Ser. in Solid-State Sciences, Vol. 164, Eds C Lacroix, P Mendels, F Mila) (Berlin: Springer, 2011) p. 365, DOI:10.1007/978-3-642-10589-0_14
38. Sachdev S *Quantum Phase Transitions* 2nd ed. (Cambridge: Cambridge Univ. Press, 2011) DOI:10.1017/CBO9780511973765
39. Dzialoshinskii I E *Sov. Phys. JETP* **5** 1259 (1957); *Zh. Eksp. Teor. Fiz.* **32** 1547 (1957)
40. Dzyaloshinsky I *J. Phys. Chem. Solids* **4** 241 (1958)
41. Moriya T *Phys. Rev. Lett.* **4** 228 (1960)
42. Moriya T *Phys. Rev.* **120** 91 (1960)
43. Borisov A B *Phys. Usp.* **63** 269 (2020); *Usp. Fiz. Nauk* **190** 291 (2020)
44. Luttinger J M, Tisza L *Phys. Rev.* **70** 954 (1946)
45. Diep H T (Ed.) *Frustrated Spin Systems* 2nd ed. (Singapore: World Scientific, 2013) DOI:10.1142/8676
46. Wolf M M, Verstraete F, Cirac J I *Int. J. Quantum Inform.* **01** 465 (2003)
47. Amico L et al. *Rev. Mod. Phys.* **80** 517 (2008)
48. Facchi P et al. *New J. Phys.* **12** 025015 (2010)
49. Zubarev D N *Sov. Phys. Usp.* **3** 320 (1960); *Usp. Fiz. Nauk* **71** 71 (1960)
50. Barabanov A F, Mikheenkov A V, Shvartsberg A V *Theor. Math. Phys.* **168** 1192 (2011); *Teor. Mat. Fiz.* **168** 389 (2011)
51. Savary L, Balents L *Rep. Prog. Phys.* **80** 016502 (2017)
52. Manousakis E *Rev. Mod. Phys.* **63** 1 (1991)
53. Siurakshina L, Ihle D, Hayn R *Phys. Rev. B* **64** 104406 (2001)
54. Mikheyenkov A V, Barabanov A F, Kozlov N A *Phys. Lett. A* **354** 320 (2006)
55. Barabanov A F, Mikheyenkov A V, Belemuk A M *Phys. Lett. A* **365** 469 (2007)
56. Mikheyenkov A V, Kozlov N A, Barabanov A F *Phys. Lett. A* **373** 693 (2009)
57. Härtel M et al. *Phys. Rev. B* **81** 174421 (2010)
58. Härtel M et al. *Phys. Rev. B* **87** 054412 (2013)
59. Mikheenkov A V, Shvartsberg A V, Barabanov A F *JETP Lett.* **98** 156 (2013); *Pis'ma Zh. Eksp. Teor. Fiz.* **98** 179 (2013)
60. Mikheenkov A V, Valiulin V E, Shvartsberg A V, Barabanov A F *J. Exp. Theor. Phys.* **121** 446 (2015); *Zh. Eksp. Teor. Fiz.* **148** 514 (2015)

61. Barabanov A F, Mikheenkov A V, Kozlov N A *JETP Lett.* **102** 301 (2015); *Pis'ma Zh. Eksp. Teor. Fiz.* **102** 333 (2015)
62. Mikheyenkov A V, Shvartsberg A V, Valiulin V E, Barabanov A F *J. Magn. Magn. Mater.* **419** 131 (2016)
63. Richter J, Schulenburg J, Honecker A "Quantum magnetism in two dimensions: From semi-classical Néel order to magnetic disorder," in *Quantum Magnetism* (Lecture Notes in Physics,Vol. 645, Eds U Schollwöck et al.) (Berlin: Springer, 2004) pp. 85–153, DOI:10.1007/BFb0119592
64. Fröbrich P, Kuntz P J *Phys. Rep.* **432** 223 (2006) DOI:10.1016/j.physrep.2006.07.002
65. Feldkemper S et al. *Phys. Rev. B* **52** 313 (1995)
66. Feldkemper S, Weber W *Phys. Rev. B* **57** 7755 (1998)
67. Melzi R et al. *Phys. Rev. Lett.* **85** 1318 (2000)
68. Melzi R et al.P*hys. Rev. B* **64** 024409 (2001)
69. Rosner H et al. *Phys. Rev. B* **67** 014416 (2003) DOI:10.1103/PhysRevB.67.014416
70. Manaka H et al. *Phys. Rev. B* **68** 184412 (2003)
71. Kaul E E et al. *J. Magn. Magn. Mater.* **272–276** 922 (2004)
72. Kageyama H et al. *J. Phys. Soc. Jpn.* **74** 1702 (2005)
73. Kasinathan D, Kyker A B, Singh D J *Phys. Rev. B* **73** 214420 (2006)
74. Skoulatos M et al. *J. Magn. Magn. Mater.* **310** 1257 (2007)
75. Nath R et al. *Phys. Rev. B* **78** 064422 (2008)
76. Carretta P et al. *Phys. Rev. B* **79** 224432 (2009)
77. Tsirlin A A, Rosner H *Phys. Rev. B* **79** 214417 (2009)
78. Tsirlin A A et al. *Phys. Rev. B* **80** 132407 (2009)
79. Skoulatos M et al. *Europhys. Lett.* **88** 57005 (2009)
80. Tsirlin A A et al. *Phys. Rev. B* **81** 174424 (2010)
81. Tsirlin A A et al. *Phys. Rev. B* **84** 014429 (2011)
82. Guchhait S et al. *Phys. Rev. B* **106** 024426 (2022)
83. Schmidt B, Shannon N, Thalmeier P *J. Phys. Condens. Matter* **19** 145211 (2007)
84. Plakida N "Antiferromagnetism in cuprate superconductors," in *High-Temperature Cuprate Superconductors. Experiment, Theory, and Applications* (Springer Series in Solid-State Sciences, Vol. 166) (Berlin: Springer, 2010) p. 51, DOI:10.1007/978-3-642-12633-8_3
85. Darradi R et al. *Phys. Rev. B* **78** 214415 (2008)
86. Junger I et al. *Phys. Rev. B* **70** 104419 (2004)
87. Sherman A, Schreiber M *Phys. Rev. B* **65** 134520 (2002)
88. Vladimirov A A, Ihle D, Plakida N M *Phys. Rev. B* **80** 104425 (2009)
89. Mikheenkov A V, Valiulin V E, Shvartsberg A V, Barabanov A F *J. Exp. Theor. Phys.* **126** 404 (2018); *Zh. Eksp. Teor. Fiz.* **153** 483 (2018)
90. Valiulin V E, Mikheyenkov A V, Chtchelkatchev N M, Barabanov A F *J. Phys. Condens. Matter* **31** 455801 (2019)
91. Noculak V et al. *Phys. Rev. B* **107** 214414 (2023)
92. Silva G A et al. *Phys. Rev. E* **109** 064113 (2024)
93. Izyumov Yu A *Sov. Phys. Usp.* **27** 845 (1984); *Usp. Fiz. Nauk* **144** 439 (1984)
94. Sorokin A O *J. Magn. Magn. Mater.* **479** 32 (2019)
95. Mikheyenkov A V, Valiulin V E, Barabanov A F *Physica B* **599** 412533 (2020)
96. Lewenstein M et al. *Adv. Phys.* **56** 243 (2007)
97. Bloch I, Dalibard J, Zwerger W *Rev. Mod. Phys.* **80** 885 (2008)
98. Georgescu I M, Ashhab S, Nori F *Rev. Mod. Phys.* **86** 153 (2014)
99. Fraxanet J, Salamon T, Lewenstein M "The coming decades of quantum simulation," in *Sketches of Physics*: *The Celebration Collection* (Lecture Notes in Physics, Vol. 1000, Eds R Citro et al.) (Cham: Springer, 2023) p. 85, 10.1007/978-3-031-32469-7_4
100. Tsujimoto Y et al. *J. Phys. Soc. Jpn.* **76** 063711 (2007)
101. Tsujimoto Y et al. *Phys. Rev. B* **78** 214410 (2008)
102. Yusuf S M et al. *Phys. Rev. B* **84** 064407 (2011)
103. Ritter C et al. *Phys. Rev. B* **88** 104401 (2013)
104. Zwanzig R *J. Chem. Phys.* **33** 1338 (1960)
105. Zwanzig R *Phys. Rev.* **124** 983 (1961)
106. Zwanzig R *Annu. Rev. Phys. Chem.* **16** 67 (1965)
107. Zwanzig R, Nordholm K S J, Mitchell W C *Phys. Rev. A* **5** 2680 (1972)
108. Mori H *Prog. Theor. Phys.* **33** 423 (1965)
109. Mori H *Prog. Theor. Phys.* **34** 399 (1965)
110. Tserkovnikov Yu A *Theor. Math. Phys.* **7** 511 (1971); *Teor. Mat. Fiz.* **7** 250 (1971)
111. Tserkovnikov Yu A *Theor. Math. Phys.* **49** 993 (1981); *Teor. Mat. Fiz.* **49** 993 (1981)
112. Sherman A *Phys. Lett. A* **337** 435 (2005)
113. Plakida N M *Theor. Math. Phys.* **168** 1303 (2011); *Teor. Mat. Fiz.* **168** 518 (2011)
114. Rudoy Yu G *Theor. Math. Phys.* **168** 1318 (2011); *Teor. Mat. Fiz.* **168** 536 (2011)
115. Mikheenkov A V, Barabanov A F *J. Exp. Theor. Phys.* **105** 347 (2007); *Zh. Eksp. Teor. Fiz.* **132** 392 (2007)
116. Barabanov A F, Maksimov L A *Phys. Lett. A* **207** 390 (1995)
117. Kastner M A et al. *Rev. Mod. Phys.* **70** 897 (1998)
118. Plakida N "Theoretical models of high-T_C superconductivity," in *High-Temperature Cuprate Superconductors*: *Experiment, Theory, and Applications* (Springer Series in Solid-State Sciences, Vol. 166) (Berlin: Springer, 2010) p. 377, DOI:10.1007/978-3-642-12633-8_7
119. Kugel' K I, Khomskii D I *Sov. Phys. JETP* **37** 725 (1973); *Zh. Eksp. Teor. Fiz.* **64** 1429 (1973)
120. Kugel' K I, Khomskii D I *Sov. Phys. Usp.* **25** 231 (1982); *Usp. Fiz. Nauk* **136** 621 (1982)
121. Saitoh E et al. *Nature* **410** 180 (2001)
122. Grüninger M et al. *Nature* **418** 39 (2002)
123. Saitoh E et al. *Nature* **418** 40 (2002)
124. Ishihara S et al. *New J. Phys.* **7** 119 (2005)
125. Chen Y et al. *Phys. Rev. B* **75** 195113 (2007)
126. You W-L, Oleś A M, Horsch P *Phys. Rev. B* **86** 094412 (2012)
127. Brzezicki W, Dziarmaga J, Oleś A M *Phys. Rev. Lett.* **112** 117204 (2014)
128. You W-L, Horsch P, Oleś A M *Phys. Rev. B* **92** 054423 (2015)
129. Gotfryd D et al. *Phys. Rev. Res.* **2** 013353 (2020)
130. Mohapatra S et al. *J. Phys. Condens. Matter* **35** 045801 (2023)
131. Valiulin V E et al. *Phys. Rev. B* **102** 155125 (2020)
132. Valiulin V E et al. *SciPost Phys. Core* **6** (2) 025 (2023)
133. Kagan M Yu, Kugel' K I, Mikheenkov A V, Barabanov A F *JETP Lett.* **100** 187 (2014); *Pis'ma Zh. Eksp. Teor. Fiz.* **100** 207 (2014)
134. Valiulin V E, Mikheenkov A V, Kugel' K I, Barabanov A F *JETP Lett.* **109** 546 (2019); *Pis'ma Zh. Eksp. Teor. Fiz.* **109** 557 (2019)
135. Pati S K, Singh R R P, Khomskii D I *Phys. Rev. Lett.* **81** 5406 (1998)
136. Lundgren R, Chua V, Fiete G A *Phys. Rev. B* **86** 224422 (2012)
137. Laurell P et al. *Adv. Quantum Technol.* **8** 2400196 (2025) DOI:10.1002/qute.202400196
138. Vedeneev S I *Phys. Usp.* **64** 890 (2021); *Usp. Fiz. Nauk* **191** 937 (2021)
139. Barabanov A F, Maksimov L A, Mikheenkov A V *JETP Lett.* **74** 328 (2001); *Pis'ma Zh. Eksp. Teor. Fiz.* **74** 362 (2001)
140. Barabanov A F, Mikheenkov A V, Belemuk A M *JETP Lett.* **75** 107 (2002); *Pis'ma Zh. Eksp. Teor. Fiz.* **75** 118 (2002)
141. Barabanov A F, Maksimov L A, Mikheyenkov A V "Spin polaron in the cuprate superconductors: Interpretation of the ARPES results," in *Spectroscopy of High-T_C Superconductors. A Theoretical View* (Ed. N M Plakida) (London: Taylor and Francis, 2003) p. 1
142. Val'kov V V, Dzebisashvili D M, Korovushkin M M, Barabanov A F *Phys. Usp.* **64** 641 (2021); *Usp. Fiz. Nauk* **191** 673 (2021)
143. Plakida N M *J. Supercond. Nov. Magn.* **28** 1309 (2015)
144. Plakida N M *Physica C* **531** 39 (2016)
145. Plakida N M, Oudovenko V S *J. Supercond. Nov. Magn.* **29** 1037 (2016)
146. Plakida N M *Physica C* **549** 69 (2018)
147. Plakida N M *Phys. Part. Nucl.* **51** 797 (2020)
148. Shimahara H, Takada S *J. Phys. Soc. Jpn.* **61** 989 (1992)
149. Vladimirov A A, Ihle D, Plakida N M *Theor. Math. Phys.* **152** 1331 (2007); *Teor. Mat. Fiz.* **152** 538 (2007)
150. Vladimirov A A, Ihle D, Plakida N M *Eur. Phys. J. B* **92** 135 (2019)
151. Tung N D, Vladimirov A A, Plakida N M *Physica C* **587** 1353900 (2021)
152. Bulaevskii L N, Nagaev E L, Khomskii D I *Sov. Phys. JETP* **27** 836 (1968); *Zh. Eksp. Teor. Fiz.* **54** 1562 (1968)
153. Trugman S A *Phys. Rev. B* **37** 1597 (1988)
154. Inui M, Doniach S, Gabay M *Phys. Rev. B* **38** 6631 (1988)
155. Barabanov A F, Zhasinas E V *Phys. Lett. A* **193** 191 (1994)
156. Barabanov A F, Beresovsky V M, Žasinas E *Phys. Rev. B* **52** 10177 (1995)
157. Savchenkov P S, Barabanov A F *J. Magn. Magn. Mater.* **521** 167505 (2021)
158. Nemkovski K S et al. *Phys. Procedia* **42** 18 (2013)
159. Lüscher A, Läuchli A M *Phys. Rev. B* **79** 195102 (2009)
160. Winterfeldt S, Ihle D *Phys. Rev. B* **56** 5535 (1997)
161. Winterfeldt S, Ihle D *Phys. Rev. B* **59** 6010 (1999)
162. Vladimirov A A, Ihle D, Plakida N M *Eur. Phys. J. B* **87** 112 (2014)
163. Nussinov Z, van den Brink J *Rev. Mod. Phys.* **87** 1 (2015)
164. Vladimirov A A, Ihle D, Plakida N M *Eur. Phys. J. B* **88** 148 (2015)